



HAL
open science

Dynamic Crystallization of a Haplogranitic Melt - Application to Pegmatites

Karine Devineau, Rémi Champallier, Michel Pichavant

► **To cite this version:**

Karine Devineau, Rémi Champallier, Michel Pichavant. Dynamic Crystallization of a Haplogranitic Melt - Application to Pegmatites. *Journal of Petrology*, 2020, 61 (5), pp.egaa054. 10.1093/petrology/egaa054 . insu-02613285

HAL Id: insu-02613285

<https://insu.hal.science/insu-02613285>

Submitted on 20 May 2020

HAL is a multi-disciplinary open access archive for the deposit and dissemination of scientific research documents, whether they are published or not. The documents may come from teaching and research institutions in France or abroad, or from public or private research centers.

L'archive ouverte pluridisciplinaire **HAL**, est destinée au dépôt et à la diffusion de documents scientifiques de niveau recherche, publiés ou non, émanant des établissements d'enseignement et de recherche français ou étrangers, des laboratoires publics ou privés.

Dynamic Crystallization of a Haplogranitic Melt - Application to Pegmatites

Karine Devineau^{1*}, Rémi Champallier² and Michel Pichavant²

¹CRPG UMR 7358 CNRS, Univ. Lorraine, F-54506 Vandœuvre-lès-Nancy, France

²ISTO UMR 7327 CNRS, Univ. Orléans, F-45071 Orléans, France

*Corresponding author. E-mail: karine.devineau@univ-lorraine.fr

ABSTRACT

Both equilibrium and dynamic crystallization experiments have been performed on a hydrous haplogranitic melt at 200 MPa to model nucleation and growth mechanisms and simulate pegmatite textures. The equilibrium results provide a reference frame (phase assemblages and compositions, liquidus and solidus temperatures and dependence with the melt H₂O concentration) to parametrize the kinetic experiments. The seven H₂O-saturated dynamic crystallization experiments followed a specific time-temperature path. After a pre-conditioning step at 800°C, charges were cooled between 3.5 and 7°C/min to 700, 660 and 600°C corresponding to ΔT of 20, 60 and 120°C. Dwell times ranged from 42 up to 1440h. Variable mineral assemblages and textures, and two types of polymineralic assemblages were obtained depending on ΔT and t . For $\Delta T = 120^\circ\text{C}$, crystallization is sequential and includes graphic quartz-alkali feldspar intergrowths characteristic of pegmatite textures. The crystallization sequence reflects nucleation and growth of kinetically-favored metastable phases and solid solution compositions from the supercooled melt. Early alkali feldspars are more K-rich than expected at equilibrium and late albites more Na-rich. The K-rich graphic texture progressively evolves to a Na-rich intergrowth texture. Melts also follow a progressive though limited sodic evolution with time. At the interface of growing alkali feldspars, melts are enriched in SiO₂ and depleted in Al₂O₃, Na₂O and, to a lesser extent, K₂O. H₂O accumulates at the interface reaching concentration levels higher (by 1-2 wt%) than the saturation. Rejection of SiO₂ and H₂O at the interface controls the effective undercooling in the local melt and promotes rapid textural changes toward larger grain sizes at the front of graphic zones. Textural ripening takes place contemporaneously to sequential crystallization. Growth rates for quartz and alkali feldspar are tightly grouped, between 7.3×10^{-11} and 1.6×10^{-12} m s⁻¹. Textures from the dynamic crystallization experiments closely resemble natural

pegmatites but layered aplite units have not been reproduced. Our results confirm and strengthen the importance of liquidus undercooling to generate pegmatite textures.

Key words: pegmatitic textures; experimental petrology; haplogranite system; dynamic crystallization

INTRODUCTION

Granitic pegmatites are sources of critical and strategic elements and of industrial minerals and, therefore, a good understanding of their formation is essential for exploration. Probably the most specific aspect of pegmatitic rocks is their *textures*. Pegmatites are characterized by a wide textural diversity and variability. Crystals can have a large range of sizes and morphologies; both blocky euhedral and skeletal alkali feldspars can coexist in the same pegmatitic body (e.g. London & Kontak, 2012, Fig 4). Graphic and granophyric intergrowths are common; layered and comb structures can be encountered, underlining the heterogeneous and anisotropic character of pegmatite crystal morphologies and textures (e.g. Cameron *et al.*, 1949; Jahns, 1953; Jahns, 1982; Cerny, 1991).

The crystallization of granitic pegmatites has long been a matter of scientific debate. Early studies (Jahns & Burnham 1969; see also Jahns 1982) have stressed the hydrous nature of pegmatite melts. Pegmatitic textures were ascribed to the influence of a free aqueous vapor phase generated as a result of H₂O-saturation of the melt. Later, London *et al.* (1989) argued that pegmatitic textures can be obtained under H₂O-undersaturated conditions and concluded that an aqueous vapor phase is not necessary. Fenn (1974; 1977) and Swanson (1977) observed that growth rates are reduced in presence of water vapor relatively to vapor-free conditions. According to London (1992), pegmatites best correspond to products of disequilibrium crystallization through liquidus undercooling. Several experimental studies have successfully reproduced pegmatite textures (Fenn, 1977; Swanson, 1977; Fenn, 1986; London *et al.*, 1989; London, 1999; Baker & Freda, 2001; London, 2014a; Maneta & Baker, 2014; Sirbescu *et al.*, 2017; London & Morgan, 2017). Various model pegmatite melts were used including synthetic and natural, Li-, B-doped as well as undoped granitic compositions. Initial preconditioning temperatures ranged from 750°C to 1000°C, cooling rates from 3 to 50°C/min, degrees of undercooling from 50 up to 400°C and dwell times from 0 to 3600 h

(London *et al.*, 1989; London 1999; Baker & Freda, 2001; London, 2014a; Maneta & Baker, 2014; London & Morgan, 2017; Sirbescu *et al.*, 2017). H₂O-saturated, H₂O-undersaturated and anhydrous conditions were investigated as well as crystals seeds in some studies (Baker & Freda, 2001; Maneta & Baker, 2014). Coarse-grained, heterogeneous and anisotropic mineral fabrics were obtained including skeletal, graphic, unidirectional, radiating, spherulitic, massive textures (Fenn, 1977; Swanson, 1977; Fenn, 1986; London *et al.*, 1989; Baker & Freda, 2001; Maneta & Baker, 2014; London & Morgan, 2017) as well as late replacement textures (Sirbescu *et al.*, 2017). Sequential crystallization, i.e. the development of texturally- and mineralogically- contrasting zones, was obtained in some studies (London, 2014a).

Although many aspects of the origin of pegmatites have been clarified from these experiments, several questions remain open. In particular, (1) the causes of textural heterogeneity need to be better understood, as illustrated by the coexistence of blocky euhedral and skeletal alkali feldspars (e.g. London, 2005, Fig. 7) or, more generally, of coarse-grained pegmatitic layers and fine-grained aplites which indicate rapid changes in nucleation and growth rates (e.g. Faure & Schiano, 2005). In addition, (2) the individual roles of H₂O and other volatiles (Li, F, B) on crystallization dynamics and textures must be resolved; most dynamic crystallization studies in the literature (see above) mix the influence of these components. (3) It is also important that the influence of the various parameters that control crystallization dynamics (e.g. degree of undercooling, cooling rate, dwell time) is explored in a systematic way so as to constrain timescales of pegmatite cooling and consolidation.

To resolve these questions, a systematic program of dynamic crystallization experiments has been undertaken in the haplogranitic (Q-Or-Ab) system. The choice of this simple system was motivated by the following reasons. (1) H₂O is the most important volatile

component in silicic magmas. Although uncertainty still remains on its concentration in pegmatite melts (Thomas & Davidson, 2012; London, 2015; Thomas & Davidson, 2015), determining the influence of H₂O alone on crystallization textures is a priority. (2) Data in the Q-Or-Ab system (e.g. Tuttle & Bowen, 1958; Holtz *et al.*, 1992) provide reference equilibrium crystal-liquid relations and facilitate parametrization of the dynamic crystallization experiments. Such experiments have been carried out previously in the Or-Ab (Fenn, 1977) and Q-Or-Ab-An (Swanson, 1977; Couch, 2003) but so far the haplogranite system has escaped investigation. (3) Quartz and alkali feldspars, essential components of pegmatites, are the only phases crystallizing in the Q-Or-Ab system. Therefore, mineralogical complexity is reduced compared to natural and doped systems which crystallize phases such as muscovite, virgilite, zinnwaldite and petalite among others (London *et al.*, 1989; Maneta & Baker, 2014; Sirbescu *et al.*, 2017; London & Morgan, 2017), in addition to quartz and feldspars. This paper details the experimental and analytical methodologies as well as background data on equilibrium crystal-liquid relations for a near-minimum Q-Or-Ab melt composition. Results of H₂O-saturated dynamic crystallization experiments are presented and discussed. Equivalent H₂O-undersaturated experiments will be presented in a subsequent paper.

EXPERIMENTAL AND ANALYTICAL METHODS

Starting material

All experiments were performed on a single haplogranitic glass close to the minimum of the 200 MPa H₂O-saturated haplogranite system according to Holtz *et al.* (1992). The chosen glass composition is globally appropriate for a pegmatite melt (granitic composition and representative K/Na ratio) and is very close to the composition Q₃₀Or₃₀Ab₄₀ previously investigated in detail by Holtz *et al.* (1992). The glass was made from a gel prepared using TEOS (tetraethylorthosilicate), aluminium nitrate and sodium and potassium carbonates. After

drying, the gel was fused at 1 atm and 1400°C in welded Pt capsules for approximately 4h. Two cycles of melting and grinding were performed to improve its chemical homogeneity. Electron microprobe analyses of the glass (Table 1) yield a normative composition with 30% Qtz, 32% Or, 38% Ab (abbreviated Q₃₀Or₃₂Ab₃₈) and a slight (< 1%) excess of Na, counted as Na₂SiO₃.

Experimental strategy

Two types of experiments were carried out. First, equilibrium experiments were performed to assess liquidus temperatures and their dependency with the melt H₂O concentration for the Q-Or-Ab composition studied. Procedures essentially identical to Holtz *et al.* (1992) were followed and are briefly recalled below. Second, dynamic crystallization experiments were performed using a specific time-temperature path (Fig. 1) which comprises successively (i) an initial pre-conditioning step (always at 800°C for 120 hours), (ii) a cooling step where temperature is lowered down to the desired experimental value (T_{Exp}) and (iii) a dwell at T_{Exp} . This time-temperature path involves four parameters. T_{Exp} was varied between 700 and 600°C, the degree of undercooling or difference between the liquidus temperature T_L and T_{Exp} (ΔT) ranged from 20 to 120°C and the dwell time (td) lasted for 42 up to 1440h. The rate of the cooling step ($\delta T/\delta t$) slightly changed with the furnace and ΔT . However, it was kept between 3.5 and 7°C/min during the first part of the cooling ramp, decreasing to smaller values (~1-2 and then ~0.1-0.4 °C/min) during the last and final parts of the ramp.

Experimental methods

Both H₂O-saturated (equilibrium and dynamic crystallization) and H₂O-undersaturated (equilibrium) experiments were performed using respectively H₂O and H₂O-CO₂ fluid mixtures (e.g. Pichavant, 1987; Holtz *et al.*, 1992). Doubly distilled deionized H₂O and

$\text{Ag}_2\text{C}_2\text{O}_4$ were used as H_2O and CO_2 sources, respectively. For the H_2O -saturated experiments [$X_{\text{H}_2\text{O}} \text{ initial} = \text{H}_2\text{O}/(\text{H}_2\text{O}+\text{CO}_2)_{\text{initial}} = 1$, see Holtz *et al.*, 1992], all experiments initially contained 10 wt% fluid (pure H_2O), i.e. an amount of H_2O sufficiently high to saturate the melt at 200 MPa (see below). For the H_2O -undersaturated experiments [$X_{\text{H}_2\text{O}} \text{ initial} = 0.85, 0.7$], the same proportion of 10 wt% fluid ($\text{H}_2\text{O} + \text{CO}_2$) was kept. The solubility of CO_2 in the silicate melt is very small under our conditions (Holloway, 1976) and, therefore, a H_2O - CO_2 fluid mixture is present in those experiments. This fluid mixture imposes $a_{\text{H}_2\text{O}} < 1$ and so the equilibrium melt has a H_2O concentration $<$ saturation. H_2O -undersaturated but fluid-absent conditions were also tested to check the influence of gas bubbles on crystallization textures. To do so, only H_2O was added to the starting glass (as for the H_2O -saturated capsules) but the amount of H_2O was less than required for H_2O -saturation. All charges consisted of 30 mg of glass crushed to a grain size $< 50 \mu\text{m}$ plus the required amounts of the different fluid components as detailed above. These were loaded in Au capsules (15 mm long; $\varnothing_{\text{ext}}=2.9 \text{ mm}$; $\varnothing_{\text{int}}=2.5 \text{ mm}$) which were welded shut. Capsules were reweighed after 24h at 120°C to ensure that no leaks occurred.

Experimental apparatus and procedure

Experiments were performed at ISTO (Université d'Orléans, France) between 600 and 900°C and at 200 MPa using both cold-seal and internally heated pressure vessels pressurized with Ar. Rapid-quench cold-seal pressure vessels were used at temperatures up to 800°C (Rudert *et al.*, 1976; Pichavant, 1987). For each vessel-furnace pair, the hot-spot zone was determined under pressure by using two internal sheathed chromel-alumel thermocouples calibrated against melting of NaCl and LiCl. The overall maximum error on the recorded temperatures is less than $\pm 5^\circ\text{C}$. Pressure was measured with a Heise-Bourdon tube gauge (uncertainty ± 20 bars) and was checked periodically. In most experiments, several capsules placed side by side

were run together. At the end of the experiment, the vessel was held vertically and capsules fell in the cold part (drop quench). At 850 and 900°C, an internally heated pressure vessel working vertically was used. Pressure was recorded with a transducer calibrated against a Heise-Bourdon tube gauge (uncertainty ± 20 bars). A molybdenum furnace was used and temperature was monitored with two type K thermocouples (overall uncertainty $\pm 5^\circ\text{C}$). Runs were terminated by switching off the power of the furnace. Quench (time necessary for temperature to fall $< 300^\circ\text{C}$) lasted for ~ 3 min and the pressure drop during cooling was compensated by pumping Ar into the vessel (isobaric quench). After a check for leaks by weighing, the capsules were sectioned, mounted in epoxy and prepared as polished sections.

Analytical methods

Textures and crystal morphologies were studied microscopically on polished sections by SEM backscattered electron (BSE) imaging using a JEOL JSM 7600F microscope operating at 15 kV accelerating voltage (SCMEM-UMR 7359 GeoRessources, Université de Lorraine, France). A JEOL JSM-6510 SEM equipped with a Bruker Quantax EDS (CRPG-UMR 7358, Université de Lorraine, France) and operated under a 15 kV beam voltage and a 24 pA current served for the analysis of certain small size feldspars. Major element analyses of most minerals and glasses were obtained using a Cameca SX100 electron microprobe (SCMEM-UMR 7359 GeoRessources, Université de Lorraine, France). Operating conditions were 15 kV accelerating voltage, 6 nA beam current, 10 s counting times on Si and Al peaks and 8 s counting times on Na and K peaks. Standards included natural albite for Na and Si, orthoclase for K and synthetic Al_2O_3 for Al. Phi-rhoZ correction procedures were applied. A focused beam (size 1 μm) was used for quartz and feldspars. Glasses were analyzed with a defocused beam (size 10 μm) to minimize the migration of alkali, and both single point (spot) analyses and compositional profiles (15 μm step) were obtained. Secondary glass standards of known

H₂O contents (measured by either SIMS or IR, see below) were systematically analyzed together with the experimental samples to determine correction factors for the alkalis (e.g. Pichavant, 1987). Na₂O and K₂O concentrations of secondary standard glasses were fitted as a function of the glass H₂O concentration and correction factors determined. For H₂O-saturated conditions, correction factors were +3-14% for Na₂O and +0.1-1.3% for K₂O depending on the analytical session.

Phase proportions in the equilibrium experiments were calculated both by mass-balance and with the lever rule. The mass-balance calculations used the electron microprobe compositions of the dry starting glass, of experimental glasses (after corrections of the alkali) and of alkali feldspars. The ternary Q-Or-Ab phase diagram was constructed by projecting the normative compositions of the starting glass and experimental glasses and the composition of alkali feldspars; phase proportions were obtained directly by applying the lever rule in the ternary diagram.

Analysis of H₂O

Five selected glasses, designated below as secondary standard glasses, were analyzed for H₂O by Fourier Transform Infrared Spectroscopy (FTIR) and secondary ion mass spectrometry (SIMS).

IR analyses were performed using a Nicolet 6700 spectrometer and a Continuum IR microscope equipped with an IR source, a KBr beamsplitter and a liquid nitrogen cooled MCT/A detector (ISTO-UMR 7327, Université d'Orléans, France). The spot size was 50 μm. FTIR spectra were accumulated for 128 scans at a resolution of 4 cm⁻¹ on doubly polished glasses with thicknesses from 43 to 108 μm (+/- 1-2 μm) as measured with an optical microscope. The bulk concentration of water was obtained by summing the concentrations of OH and H₂O species as determined from the intensities of the 4500 and 5200 cm⁻¹ absorption

bands (measured with a straight base line) using the Lambert-Beer law. Molar absorption coefficients (ϵ) of $1.79 (\pm 0.021) \text{ L mol}^{-1} \text{ cm}^{-1}$ for H_2O and $1.56 (\pm 0.021) \text{ L mol}^{-1} \text{ cm}^{-1}$ for OH were used (Behrens & Nowak, 2003). Densities of experimental hydrous glasses were estimated from the density of the volatile-free reference glass HPG-8 (of composition similar to the $\text{Q}_{30}\text{Or}_{32}\text{Ab}_{38}$ starting glass) measured on a Mettler balance equipped with a density accessory kit ($\rho = 2.282 \pm 0.006$). For hydrous glasses, a linear dependency between the density and the H_2O concentration (Richet *et al.*, 2000) was assumed.

SIMS measurements included both single point (spot) analyses and compositional profiles (10 μm step). The spot analyses were performed on a Cameca IMS 1280 HR2 ion probe (CRPG, CNRS-INSU, Université de Lorraine, France) and the profiles on a Cameca IMS 1270E7 ion probe (CRPG, CNRS-INSU, Université de Lorraine, France). Both ion probes used a Cs^+ primary beam focused onto a 10 μm diameter spot with a 1.5 nA intensity. The electron gun was used with an HV adjusted by limiting the H^- emission to below 1000 cps. Negative secondary ions $^{16}\text{O}^-$, $^{16}\text{OH}^-$ and $^{28}\text{Si}^-$ were counted. For each measurement, the sample was pre-sputtered for 2 min, the secondary beam position in the aperture field and the magnetic field checked automatically, and 8 cycles were acquired for a total of 12 min. For spot analyses, five HPG-8 glasses of different H_2O contents as determined by Karl Fischer titration (Martel *et al.*, 2000; C. Martel pers.com.) were used as standards. Calibration curves were determined by plotting the H_2O content of standards against their measured $^{16}\text{OH}^-/^{16}\text{O}^-$. For profiles, glasses with H_2O contents determined from spot analyses were used as standards and calibration curves constructed as above.

Both the FTIR and spot SIMS results were used to estimate H_2O concentrations "by difference" (BD). To do so, glasses analyzed by IR and SIMS (Table S1 and Fig. S1) were analyzed by electron microprobe and their analytical totals (after corrections of the alkali) plotted as a function of their glass H_2O contents. For each microprobe session, empirical

calibrations relating the summation deficiency (100 - analytical total) with the glass H₂O content were constructed from either the IR or the SIMS H₂O concentration data ("by difference"-IR and "by difference"-SIMS), and applied to estimate the concentration of H₂O in experimental glasses.

RESULTS

Glass H₂O concentrations

The H₂O contents of the secondary standard glasses determined with the four methods (IR, SIMS, "by difference"-IR, "by difference"-SIMS) range from ~3.5 to ~7 wt%. (Table S1; Fig. S1). The results are referenced against the Karl-Fischer titration (KFT) data of Holtz *et al.* (1992). The SIMS data yield H₂O concentrations close (within 1-10% relative) to reference data, both for the H₂O-saturated and the H₂O-undersaturated glasses; duplicates are almost identical (5.82 vs. 5.85 wt% H₂O, Table S1; Fig. S1). In comparison, the IR H₂O concentration data are more dispersed and they commonly exceed (by up to 38% relative) both the SIMS measurements and the KFT data. We attribute the relatively poor performance of our IR results to the presence of numerous fluid bubbles in the secondary standard glasses. The "by difference"-SIMS results little depart from reference data (2-14% relative) whereas higher deviations (20-35% relative) are observed for "by difference"-IR values. Therefore, estimation of the H₂O content of experimental glasses below is based on the "by difference"-SIMS rather than the "by difference"-IR method.

Phase equilibrium results

Conditions and results of the phase equilibrium experiments are listed in Table S2 and the phase relations are represented in Fig. S2. Liquid (silicate melt, L), alkali feldspar (AF) and quartz (Q) are present. Alkali feldspars form numerous small crystals with a tabular

morphology (Fig. 2a). Experimental charges observed in 2D polished surfaces on BSE-SEM images show that crystal nucleation appears homogenous whatever the H₂O content (wt%). Vapor (V) is present in all charges as ascertained by fluid inclusions (petrographic examination) and open vesicles (SEM imaging). However, in Fig. S2, the vapor-present stability fields (L+V, L+AF+V) are defined only from the four H₂O-saturated charges (i.e. V represents pure H₂O) to highlight the range of H₂O contents at saturation (5.8-6.8 wt%, Table S2). Yet, a H₂O-CO₂ vapor is also present in the CO₂-bearing H₂O-undersaturated charges. Upon decreasing temperature at constant melt H₂O concentration (or decreasing melt H₂O concentration at constant temperature), alkali feldspar appears as the liquidus phase and is followed by quartz, consistent with previous results (Holtz *et al.*, 1992) on compositions such as Q₃₀Or₃₂Ab₃₈. The H₂O-saturated liquidus is bracketed between the 700 and 750°C charges and a liquidus temperature of 720°C is estimated, in agreement with results of forward and reversal experiments on compositions near Q₃₀Or₃₂Ab₃₈ (Holtz *et al.*, 1992). When lowering the melt H₂O concentration, the liquidus temperature progressively increases, reaching > 850°C for < 4 wt% H₂O. The 700°C Xⁱⁿ_{H₂O}=0.7 charge 11 contains no melt (Table S2) indicating that the solidus has been overstepped.

Dynamic crystallization experiments

Conditions and results of the dynamic crystallization experiments are summarized in Table 2. Three experiments were performed at $T_{Exp} = 700^{\circ}\text{C}$ ($td = 42, 360$ and 648h), corresponding to $\Delta T = 20^{\circ}\text{C}$ (Fig. 1), one at $T_{Exp} = 660^{\circ}\text{C}$ ($\Delta T = 60^{\circ}\text{C}$) for $td = 1320\text{h}$ and three at $T_{Exp} = 600^{\circ}\text{C}$ ($\Delta T = 120^{\circ}\text{C}$) for 120, 552 and 1440h. Cooling rates (from ~5 to ~7°C/min, Table 2) were essentially identical between experiments. Pegmatitic textures are observed in the two longest experiments at 600°C (43-4b, 33-4c, Table 2) which correspond to the highest degree of undercooling ($\Delta T = 120^{\circ}\text{C}$) in our dataset. It is worth emphasizing that the two 660 and 600°C

experiments were both performed below the H₂O-saturated solidus temperature of the Q₃₀Or₃₂Ab₃₈ composition (~685°C Holtz *et al.*, 1992; Fig. 1). Therefore, these charges simulate crystallization of highly supercooled metastable melts.

Phase assemblages, crystal morphologies and textures

Phases encountered in the dynamic crystallization charges include liquid, alkali feldspars, quartz and vapor, the latter clearly marked in all charges by the occurrence of numerous vesicles up to ~50 µm homogeneously distributed in glass (Fig. 2b). Liquid is generally abundant except in 33-4c where crystallization essentially went to completion (Table 2). Alkali feldspar crystallizes from 660°C and below (i.e. at minimum 60°C lower than in equilibrium charges, Fig. S2) and quartz only at 600°C (i.e. at minimum ~90°C lower than in equilibrium charges, Holtz *et al.*, 1992), indicating important crystallization delays in the dynamic experiments. Alkali feldspar is mostly homogeneous and relatively K-rich or K-Na intermediate, but it also shows exsolutions to K-rich and Na-rich streaks/domains (see below). A Na-rich alkali feldspar (albite) is also present, either as a homogeneous phase or as exsolutions (see below).

Characteristic crystal morphologies and sizes encountered in the dynamic experiments, as observed in 2D polished surfaces on BSE-SEM images, are reported in Table 2 and detailed in Table 3. Both alkali feldspars and quartz occur with various habits and the charges, especially 43-4b and 33-4c, demonstrate impressive textural variability. We acknowledge that the crystal morphologies and mutual relationships between phases in 2D sections may not always correspond to the 3D reality. In the equilibrium charges, alkali feldspar crystallizes as numerous and small (5 x 2 µm, Table 3) *tabular* phases (AF-tab, Fig. 2a). In the dynamic crystallization charges, alkali feldspar appears generally as large crystals with a *skeletal* morphology (AF-sk, Fig. 2b; Table 3) and most hollows are infilled with dendritic

morphologies. Composite, segmented, commonly branched and curved alkali feldspars designated as *fan* crystals (AF-f, Fig. 2c; Table 3) are also encountered and include coarse (large blocky) and rough (irregularly surfaced) habits. Fan alkali feldspars are all Na-rich, which further distinguishes them from the other alkali feldspar morphological types that all correspond to K-rich to K-Na intermediate compositions (see below). Large filled alkali feldspars crystals with well-developed faces and euhedral shapes are designated as *polygonal* (AF-pol, Fig. 2d; Table 3). Individual polygonal alkali feldspars sometimes form aggregates of larger sizes designated as megacrysts below. For quartz, morphologies include two main types, *euhedral* and *anhedral*. The former crystals have well-developed faces either morphologically complex (Q-c, Table 3) or large and prismatic (Q-p, Fig. 2e; Table 3). The latter crystals lack well-developed faces and geometrical shape (Q-an, Fig. 2f; Table 3).

Three types of polymineralic associations commonly occur (Table 4). Two (the *graphic texture*, GT and the *polymineralic assemblage*, PA) involve alkali feldspars and quartz mineral associations. The classical *graphic texture* is marked by micrometric, crystallographically controlled, quartz-feldspar intergrowths (Fenn, 1986; Lentz & Fowler, 1992; Ikeda *et al.*, 2000; Maneta & Baker, 2014; Xu *et al.*, 2015; Fig. 3a) with alkali feldspars being dominantly K-rich to K-Na intermediate. The *polymineralic assemblage* (Table 4) is characterized by very small crystals (< 1 μm , so smaller than the *graphic texture*) and lack of crystallographic organization at the scale of observation (Fig. 3b). Another difference is that the *polymineralic assemblage* appears darker than the *graphic texture* in BSE imaging indicating that the alkali feldspar is Na-rich. The third texture (*perthitic texture*, AF-pt, Table 4) corresponds to the exsolution of homogeneous alkali feldspar to respectively K- and Na-rich streaks or domains (e.g. Smith & Brown, 1988; Lee *et al.*, 1995; Fig. 3c).

Time evolution and mineralogical and textural zonation

The three experiments at $T_{Exp} = 600^{\circ}\text{C}$ ($\Delta T = 120^{\circ}\text{C}$) allow to follow the development of crystallization in 2D sections as the run duration (td) is progressively increased. In the $td = 120\text{h}$ charge, the melt is barely crystallized, only one alkali feldspar crystal of skeletal type was found. In the 552h charge cut along its entire length, the whole half charge (Fig. 4a) shows that crystallization has progressed significantly. Approximately half of the charge is crystallized, both along the rims near the capsule walls and in the middle of the glass bead (Fig. 4a). The 1440h charge failed to be cut entirely and broke into several fragments. Those shown in Fig. 5 are randomly oriented and a representative sampling of textural relations is available. They appear entirely crystallized.

In the $td = 552\text{h}$ charge, radial crystalline aggregates of several $100\ \mu\text{m}$ in diameter are observed (Fig. 4a and b). Some are isolated (entirely surrounded by glass) and others are in mutual contact (arrows in Fig. 4a). Given the dispersion of the aggregates across the entire charge and the lack of heterogeneities (bubbles, capsule fragments) in the aggregates, nucleation appears to be homogeneous. Crystallization started in *inner parts* of aggregates made up of individual crystals (alkali feldspars \gg quartz) embedded in a mostly graphic texture (Fig. 4b), the same texture being also observed inside alkali feldspar crystals (Fig. 4c). Alkali feldspar is mostly of skeletal ($L = 27\text{-}118\ \mu\text{m}$, $l = 9\text{-}29\ \mu\text{m}$, Table S3, Fig. 4c), more rarely of polygonal ($L = 14\text{-}80\ \mu\text{m}$, $l = 9\text{-}30\ \mu\text{m}$, Table S3) or of mixed polygonal-skeletal type. The skeletal morphology is encountered all along from the core to the rim of the aggregates, sometimes extending to crystals that appear isolated in the surrounding glass (Fig. 4b) in 2D view. However, in most cases, skeletal change to fan morphologies ($L = 30\text{-}113\ \mu\text{m}$, $l = 6\text{-}66\ \mu\text{m}$, Table S3) near aggregate rims, the transition between the two types being easily followed since skeletal and fan alkali feldspars have contrasting compositions, respectively K- and Na-rich (Fig. 4d). Additionally, in aggregate rims, only a few polygonal alkali feldspars are present (Fig. 4a) and dark streaks appear in skeletal crystals suggesting

exsolution of Na-rich feldspar and development of the perthitic texture (Fig. 4e). Exceptionally, megacrysts (large polygonal alkali feldspars aggregates, 500 x 200 μm) are observed (Fig. 4a) and pass to rough fan morphologies and Na-rich compositions at their rim. Quartz mainly occurs as individual crystals regularly distributed from the core to the rim of the aggregate. Both anhedral (Q-an in Fig. 4c and f) and euhedral with complex morphologies (Q-c in Fig. 4b and c) crystals are encountered but, overall, the anhedral type predominates. Crystal sizes are variable ($L = 3\text{-}68$ and $4\text{-}135$ μm and $l = 2\text{-}34$ and $1\text{-}40$ μm for the Q-an and Q-c morphologies respectively, Table S3). In the inner part, no residual liquid is left (at the scale of SEM observations). As the aggregate rim is approached (at distances < 30 μm from the surrounding glass), the graphic texture becomes replaced by a polymineralic assemblage. The transition between the two quartz-feldspar associations is progressive and no sharp boundary is apparent (Fig. 4f). In BSE imaging, this transition is marked by an overall darkening of the polymineralic assemblage and a decrease in grain size (Fig. 3a and b) making identification of individual mineral phases difficult. This transition, which marks the boundary between the inner and *transitional* parts of the radial aggregates, is outlined on Fig. 4b.

The $td = 1440\text{h}$ charge illustrates a final crystallization stage which extends the radial organization identified in the 552h charge. The core-rim mineralogical and textural zonation is more sharply marked and three parts, *inner*, *transitional* and *outer* can be defined (Fig. 5b). The *inner* part corresponds to the core of crystal aggregates and is made of individual alkali feldspars and quartz enclosed in graphic texture, as in the 552h charge. No melt is observed between crystals. Alkali feldspars include the skeletal ($L = 16\text{-}119$ μm , $l = 5\text{-}44$ μm) and polygonal ($L = 5\text{-}60$ μm , $l = 4\text{-}37$ μm) types and crystal sizes (Table S3) are generally similar to those in the 552h charge. However, polygonal morphologies appear dominant and fan crystals are absent although they might reside undetected in the transitional part (see below).

Exsolved alkali feldspars with the perthitic texture are numerous and well-developed and a few large megacrysts (900 x 300 μm) can be observed (Fig. 5a). Quartz morphologies and sizes (Table S3) are also essentially the same than in the 552h charge. They include the anhedral (L = 4-29 μm , l = 3-16 μm) and the euhedral with complex morphologies (L = 30-84 μm , l = 13-70 μm) crystals, the latter sometimes associated with polygonal alkali feldspars (Fig. 5b). The *transitional* part consists of the polymineralic assemblage (thickness 50-150 μm) more extensively developed than in the 552h charge and disconnected from the more internal graphic texture (Fig. 5b). Polygonal, skeletal and perthitic alkali feldspars, together with euhedral quartz with complex morphologies and anhedral quartz occur in association with this fine-scale polymineralic assemblage (Figs. 5b and 3b). Variations in grey levels suggest mineral and chemical heterogeneities at the infra-micrometric scale except for the presence of larger Na-rich alkali feldspars (Fig. 3b). The *outer* part is coarsely crystallized with large euhedral prismatic quartz (up to 250 x 150 μm) showing well faceted prisms and pyramidal terminations (Q-p in Fig. 5b). Alkali feldspar (30 x 50 μm) has a well-developed perthitic texture (Fig. 5b) and Carlsbad twins. Textural habits in this zone suggest growth in free, presumably vapor-filled, space.

Alkali feldspar compositions

Representative electron microprobe analyses of alkali-feldspars are detailed in Table 5. In the equilibrium experiments (700°C H₂O-saturated charge 9, Table S2), alkali feldspar is relatively K-rich (Ab₃₄Or₆₆) and in good agreement with previous data (Holtz *et al.*, 1992). In the dynamic crystallization experiments, alkali feldspar compositions at 660°C are constant (Ab₂₆Or₇₄) whatever the texture and more potassic than at 700°C in the equilibrium experiment (Fig. 6). At 600°C for 120h, only a few analyses (Ab₂₄Or₇₆) are available. For 552h, skeletal and polygonal alkali feldspar compositions are both variable and cover

approximately the same ranges, $\text{Ab}_{23-46}\text{Or}_{77-54}$ and $\text{Ab}_{23-37}\text{Or}_{77-63}$, respectively (Fig. 6). In comparison, fan crystals yield sub-homogeneous albitic compositions irrespective of their particular habit ($\text{Ab}_{90-92}\text{Or}_{10-8}$, Table 5; Fig. 6). The different contiguous polygonal alkali feldspars constituting the megacryst of Fig. 4a have the same compositions as individual polygonal alkali feldspars (Table 5). For 1440h, skeletal and polygonal alkali feldspars again have variable compositions (respectively $\text{Ab}_{26-46}\text{Or}_{74-54}$ and $\text{Ab}_{28-51}\text{Or}_{72-49}$) and in the same range as at 552h (Fig. 6). The most Na-rich compositions correspond systematically to crystals from the inner part rim, the transitional or outer part. Again the contiguous polygonal alkali feldspars constituting the megacryst of Fig. 5a have the same compositions as individual polygonal alkali feldspars (Table 5). Perthitic alkali feldspars in the outer part yield $\text{Ab}_{38}\text{Or}_{62}$ for the clear grey domains (i.e. in the middle of the ranges for skeletal and polygonal crystals) and $\text{Ab}_{92}\text{Or}_{08}$ for the dark streaks (i.e. identical to fan crystals in the 552h charge, Table 5; Fig. 6). It is important to emphasize that, perthites excepted, individual alkali feldspar crystals are homogeneous and, therefore, the variability arises from different crystals having different chemistries. Semi-quantitative SEM-EDS analysis of alkali feldspars in the fine polymineralic assemblage (Fig. 3b) yielded albitic compositions (Table 5, Fig. 6).

Composition of polymineralic associations

Difficulties with the textural identification of fine-grained mineral phases (Fig. 3) and with their individual EMPA analysis prompted us to implement a global chemical approach to better characterize the graphic texture and polymineralic assemblage. Graphic and polymineralic domains from the 552 and 1440h 600°C charges were analyzed by electron microprobe using a focused 1 μm beam size (since grain sizes are \ll 1 μm). Results were converted into normative compositions and then projected in the Q-Or-Ab diagram (Fig. 7). Representative analyses and normative compositions of mineral mixtures are reported in

Table S4. In both charges, compositions within the graphic texture are broadly granitic and overall potassic, plotting near the center of the Q-Ab-Or diagram ($Q_{27-37} Or_{33-51} Ab_{18-31}$ for 552h and $Q_{29-35} Or_{33-48} Ab_{19-36}$ for 1440h), with one Na-rich outlier ($Q_{31}Or_{24}Ab_{45}$, Fig. 7). Graphic textures have essentially constant Q contents and variable Or/Ab ratios, the most Ab-rich corresponding to analyses near polymineralic domains. Overall, the analyses correspond to mixtures between quartz and alkali feldspars in a near 35:65 proportion, consistent with textural observations (Fig. 3a). The Or/Ab ratios are those of alkali feldspars mostly between Or_{50} and Or_{75} , typical of compositions of skeletal and polygonal crystals (Table 5). In comparison, all polymineralic assemblage compositions are shifted toward the Na-rich part of the diagram (Fig. 7). The 552h data points are relatively Q-rich (up to Q_{43}), poor in normative Or (Or_{11-20} with one Or_{27} outlier) and rich in normative Ab (Ab_{45-63} with one Ab_{40} outlier). The 1440h show variable Q (Q_{8-40}), low Or (Or_{9-21} with one Or_{33} outlier) and high to very high Ab (Ab_{47-79} with one Ab_{36} outlier). The data points suggest that polymineralic domains represent mixtures in variable proportions between quartz and alkali feldspars, mainly albitic. However, albitic alkali feldspars are homogeneous and very Na-rich (Table 5) and, so, a minor proportion of a second K-rich or Na-K intermediate alkali feldspar seems necessary to account for the bulk composition of polymineralic assemblages.

Glass compositions

Representative electron microprobe analyses of experimental glasses are given in Table 6. Three groups of glasses are distinguished. (1) In the equilibrium experiments, all supraliquidus glasses have nearly identical compositions close to the $Q_{30}Or_{32}Ab_{38}$ starting material (Table 6). In the crystal-bearing charge 9, glass compositions projected in the Q-Or-Ab diagram stay localized close to the starting glass (Fig. 8a), consistent with alkali feldspars being present in low amounts (4 wt%, Table S2). (2) In the dynamic experiments, supercooled

melts in crystal-free $\Delta T = 20^\circ\text{C}$ charges are all identical and have Q-Or-Ab normative compositions overlapping with the starting glass (Fig. 8b). They have peralkaline chemistries ($0.9 < \text{A/NK} < 1$, Table 6), most probably because of slightly overestimated correction factors for the alkali (see above). (3) In the crystal-bearing $\Delta T = 60^\circ\text{C}$ and $\Delta T = 120^\circ\text{C}$ charges, glass compositions are heterogeneous (Fig. 8c).

The origin of glass heterogeneity was investigated from compositional profiles in the melt away from alkali feldspar (all of skeletal type) interfaces in the three crystal-bearing dynamic crystallization experiments at $\Delta T = 60^\circ\text{C}$ and $\Delta T = 120^\circ\text{C}$ (Table 2). Liquids are chemically zoned with SiO_2 systematically increasing and Al_2O_3 , Na_2O and K_2O all decreasing as alkali feldspar is approached (Fig. 9). For example, in the $\Delta T = 120^\circ\text{C}$ - $td = 552\text{h}$ charge, the interface melt SiO_2 increases up to ~ 81 wt % (77.6 wt% in the far-field melt) while Al_2O_3 decreases to 12.3 wt% (13.2 wt%), Na_2O to 3.5 wt% (5.1 wt%) and K_2O to 3.4 wt% (4 wt%). The width of the boundary layer is ~ 15 μm for both SiO_2 and Al_2O_3 and ~ 45 μm for Na_2O , consistent with diffusivities of melt components in the order $\text{SiO}_2 \approx \text{Al}_2\text{O}_3 < \text{Na}_2\text{O}$, as expected (Zhang & Cherniak, 2010). In the two other charges, similar widths are observed for SiO_2 although, for the other oxides, values are more scattered. Therefore, local chemical zonation, consistent with short-range diffusion in the melt at the front of growing alkali feldspars crystals, is observed. Away from alkali feldspar interfaces, melts along profiles become identical within error to far-field melts (determined by averaging individual analyses in crystal-free zones of the charge, Fig. 9). For each profile, glass compositions projected in the Q-Or-Ab diagram show a cluster near the cotectic (corresponding to melts away from alkali feldspars) and one Q-rich point that plots in the quartz primary field and corresponds to the alkali feldspar interface melt (Fig. 8c). These interface melts are metastable with respect to quartz crystallization, reminding that quartz is present only in the $\Delta T = 120^\circ\text{C}$ - $td = 552\text{h}$ charge (Table 2). Glasses near alkali feldspars also depart from the haplogranitic

A/NK=1 plane being distinctly peraluminous ($A/NK > 1.1$, Table 6) as a consequence of the marked depletion in alkali, mainly Na_2O , at the interface. Melts analyzed inside skeletal crystals also show the same evolution. Analysis of glass within an hollow alkali feldspar yielded the highest SiO_2 (~82 wt%) and A/NK (1.32) in our dataset (charge 47-3a, Table 6).

Concentration profiles in glass away from alkali feldspar interfaces have been also obtained for H_2O (Fig. 10). H_2O concentrations have been determined by difference ("by difference"-SIMS) for the same three crystal-bearing $\Delta T = 60^\circ\text{C}$ and $\Delta T = 120^\circ\text{C}$ charges. For the $\Delta T = 120^\circ\text{C}$ - $td = 552\text{h}$ charge, results have been duplicated by SIMS. In all cases, H_2O concentrations were found to increase near the alkali feldspar interface. In the $\Delta T = 60^\circ\text{C}$ charge, the interface melt H_2O concentration is ~ 7.6 wt%, vs. 6.3 wt% away from alkali feldspar and 6.5 wt% in the far-field melt. The high SiO_2 glass in the hollow alkali feldspar has a H_2O concentration of 7.1 wt% (Table 6). In the $\Delta T = 120^\circ\text{C}$ - $td = 120\text{h}$ charge, the H_2O concentration at the interface reaches 8 wt% (vs. ~6.5 wt% away from alkali feldspar and 6.2 wt% in the far-field melt). In the $\Delta T = 120^\circ\text{C}$ - $td = 552\text{h}$ charge, 10 wt% H_2O was determined at the interface vs. ~7 wt% in the far-field melt (Fig. 10c). The SIMS data did not confirm such a high amount although an interface melt H_2O concentration > 8 wt% was measured (Fig. 10d). Both the "by difference"-SIMS and SIMS data reveal a wide (~100 μm) boundary layer characterized by progressively decreasing H_2O concentrations with increasing distance from the alkali feldspar interface. Beyond that zone, H_2O concentrations along profiles and in far-field melts become identical within error. For the two other charges, the H_2O concentration profiles are more irregular and rather flat (Fig. 10a and b) probably because just a few crystals are present and so the flux of H_2O accumulated at the alkali feldspar crystallization front are smaller than in the $\Delta T = 120^\circ\text{C}$ - $td = 552\text{h}$ charge.

Superimposed to these compositional heterogeneities at the scale of the charge, compositions of glasses in crystal-bearing dynamic crystallization experiments differ from

each other. In the $\Delta T = 60^\circ\text{C}$ and $\Delta T = 120^\circ\text{C}$ - $td = 120\text{h}$ charges, glasses both far-field and away from alkali feldspar interfaces cluster on and near the starting glass (Fig. 8c), consistent with the very small amount of crystals in these two charges. In contrast, their counterparts in the $\Delta T = 120^\circ\text{C}$ - $td = 552\text{h}$ charge depart from the starting glass composition, being significantly less Or-rich (Fig. 8c). Such relatively Ab-rich residual glasses complement the crystallized portion of the charge made up of K-rich (Or₇₇₋₅₄) alkali feldspars and graphic textures (Fig. 7). This indicates that some liquid differentiation takes place in the dynamic crystallization experiments.

DISCUSSION

Dynamic vs. equilibrium crystallization

Results of the dynamic crystallization experiments contrast in many aspects with the equilibrium experiments despite both performed with the same starting composition. First-order differences concern textures, phase assemblages, proportions and compositions. For example, the polygonal, skeletal and fan-shaped alkali feldspars occur exclusively in the dynamic experiments and the tabular ones in the equilibrium experiments (Fig. 2); the former crystals are significantly larger than the latter. Polymineralic associations (the graphic texture and the polymineralic assemblage), perthitic crystals and sequential crystallization textures have been only observed in the dynamic experiments (Figs. 3-5) which are overall much more crystallized than the equilibrium ones (Figs. 2a, 4 and 5). The former are the only experiments where an albitic alkali feldspar is present (Fig. 6) and where glasses are chemically zoned (Figs. 8, 9 and 10). Residual glasses show distinct evolutions in the crystal-rich dynamic $\Delta T = 120^\circ\text{C}$ - $td = 552\text{h}$ and in equilibrium charges (Fig. 8).

These contrasting results find their origin in the respective (1) conditions (temperature, T_{Exp}) and (2) time-temperature paths in the two types of experiments. T_{Exp} are lower in the

dynamic (600 and 660°C, Table 2) than in the equilibrium (700°C, Table S2) experiments. This explains the higher crystallinities (Figs. 4 and 5) in the former than in the latter and the presence of albitic alkali feldspars (since 600°C is lower than the critical temperature of the alkali feldspar solvus, Fig. 6). The low T_{Exp} of the dynamic experiments also favors the persistence of chemical zonation in glass near alkali feldspar interfaces (Figs. 9 and 10) since diffusivities generally decrease with temperature. The time-temperature path in the dynamic experiments (Fig. 1) is known to induce melt supercooling and generate nucleation delays (Fenn, 1977; Swanson, 1977; Fenn, 1986), probably because pre-conditioning above the liquidus eliminates all nuclei formed during heating up. In comparison, for the equilibrium experiments, initially dry starting glasses were used and T_{Exp} was attained directly from room temperature (Pichavant, 1987; Holtz *et al.*, 1992). By doing so, crystal nucleation is promoted during heating since the charge passes through an intermediate temperature H₂O-undersaturated melt region where nucleation is maximized (Fenn, 1977). Therefore, the nucleation delay at T_{Exp} is greatly minimized in the equilibrium experiments.

There is, however, one specificity worth being emphasized in our dynamic crystallization experiments. The four crystal-bearing charges are for experiments carried out at T_{Exp} (660, 600°C, Table 2), i.e. lower than the solidus temperature of the starting H₂O-saturated Q-Or-Ab melt at 200 MPa (~685°C, Tuttle & Bowen, 1958; Holtz *et al.*, 1992). It follows that melts in those charges are metastable with respect to the complete solidification of a quartz-alkali feldspar mixture. This crystallization mechanism has been recognized of key importance for the development of pegmatite textures (“isothermal subsolidus crystallization”, London, 2014b). To illustrate the process, London (2014b) presented dynamic crystallization experiments performed with a Macusani glass and a dry Q-Or-Ab melt containing 3 wt% B₂O₃. Our results in the H₂O-saturated Q-Or-Ab system provide additional information of this mechanism.

Sequential crystallization processes

Below, the overall crystallization sequence in the dynamic experiments is broken down in to four successive steps that are each defined, interpreted and compared with results from previous studies.

The earliest crystallization step (I) is constrained by the $\Delta T = 20^\circ\text{C}$ and $\Delta T = 60^\circ\text{C}$ experiments and the shortest $\Delta T = 120^\circ\text{C}$ charge (Table 2; Fig. 11). Alkali feldspar did not nucleate in the $\Delta T = 20^\circ\text{C}$ charges despite td up to 648h. This is consistent with Fenn (1977) who reports charges with no alkali feldspar growth after 72 h or more at very low values of undercooling (see also Sirbescu *et al.*, 2017 for long alkali feldspar nucleation delays). For $\Delta T = 60^\circ\text{C}$, the only available long duration ($td = 1320\text{h}$) and alkali feldspar-bearing although crystal-poor charge is compatible with an incubation period in the 100-1000h range. In comparison, for $\Delta T = 120^\circ\text{C}$, alkali feldspar is present after only 120h and, so, the $\Delta T = 60$ and 120°C data are consistent with a decrease of the nucleation incubation period with the degree of undercooling (Lofgren, 1974; Fenn, 1977; London, 2014a; Sirbescu *et al.*, 2017; Fig. 11). Alkali feldspar in the $\Delta T = 120^\circ\text{C}$ - $td = 120\text{h}$ charge is the earliest grown in our experiments (since it is associated with the shortest incubation time) and it shows the skeletal morphological type only (Fig. 2b). Note that, in the $\Delta T = 60^\circ\text{C}$ charge which is also representative of early alkali feldspar crystallization stages, both skeletal and polygonal crystals coexist. However, td is much longer in this than in the $\Delta T = 120^\circ\text{C}$ experiment (1320 vs. 120h, Table 2). This suggests that the polygonal type is the product of a longer and probably more complex crystallization process than the skeletal. Fenn (1977) found skeletal type to be relatively rare in his charges when compared to tabular and spherulitic types. However, morphological trends depend on melt chemistry. Skeletal alkali feldspars similar to the ones observed in this study have been grown by Maneta & Baker (2014) from both Li-free

and Li-doped compositions (see also London, 2014a). In general, skeletal morphologies are expected at intermediate ΔT , tabular crystals at lower values, and dendritic and spherulitic crystals at higher degrees of undercooling (Lofgren, 1974; Kirkpatrick, 1975; Fenn, 1977; Swanson, 1977). Our results in the Q-Or-Ab system are in general agreement with these trends. In addition, they unambiguously demonstrate that chemical diffusion in the melt controls the growth of alkali feldspars (Kirkpatrick, 1975). Previous studies (Fenn, 1986; London *et al.*, 1989; Maneta & Baker, 2014; London & Morgan, 2017; Sirbescu *et al.*, 2017) have suggested the existence of boundary layers at the interface of growing feldspar crystals or feldspar-quartz aggregates. For example, Fenn (1986) mentioned rejection of non-feldspar components (SiO_2 and H_2O) at the interface of alkali feldspars grown from natural pegmatite melts. This is essentially the mechanism demonstrated by the major element and H_2O zonation observed at the front of skeletal crystals in this study (Figs. 9 and 10). It is important to stress that the accumulation of H_2O (in addition to SiO_2) leads to a modified distribution of the undercooling in the melt near the alkali feldspar interface (Kirkpatrick, 1975; Fig. 12).

The composition of early-crystallized alkali feldspar warrants a detailed discussion because it controls the subsequent chemical evolution and the development of mineral zonation. An important observation is that the early-crystallizing alkali feldspars in the $\Delta T = 60^\circ\text{C}-td = 1320\text{h}$ and $\Delta T = 120^\circ\text{C}-td = 120\text{h}$ charges are more potassic than the equilibrium alkali feldspar at 700°C (respectively Or_{74} and Or_{76} vs. Or_{66} , Table 5; Fig. 6). These higher Or contents cannot be explained by the lower temperatures in the dynamic than in the equilibrium experiments since, in the H_2O -saturated Q-Or-Ab system at 200 MPa, alkali feldspar coexisting at equilibrium with liquid becomes progressively less Or-rich with decreasing temperature (Fig. 13a). Deviations from equilibrium compositions have been previously noted by Parsons (1969) and Fenn (1977) for alkali feldspars grown from gels or

melts under subsolidus conditions. For bulk compositions more potassic than the minimum of the Or-Ab system, crystallized alkali feldspars were more Or-rich than their corresponding starting compositions (Parsons, 1969), as found in this study. K-rich alkali feldspar compositions ($\sim\text{Or}_{80}$) were also grown by Maneta & Baker (2014) and Sirbescu *et al.* (2017) but the lack of equilibrium data for comparison limits the interpretations. It is interesting to note that similar deviations from equilibrium compositions have been observed also for plagioclase, the An content increasing with increasing cooling rate and decreasing dwell temperature for a constant bulk melt composition (Iezzi *et al.*, 2011). Generally, phase assemblages and compositions of solid solutions formed during dynamic crystallization are interpreted using the nucleation theory (e.g. Kirkpatrick, 1983; Hammer, 2008; Iezzi *et al.*, 2008). Crystallization of a supercooled melt involves nucleation and growth of kinetically-favored metastable phases and metastable solid solution compositions. To illustrate this mechanism, metastable crystallization of a hydrous Q-Or-Ab melt is schematically represented in Fig. 13. Two situations, (1) supercooling below the liquidus and (2) supercooling below the solidus (subsolidus crystallization, London, 2014b) are considered. In case (1), a range of alkali feldspars (between AFa and AFb) which includes compositions more potassic than equilibrium (AFn vs. AF1) can nucleate and grow from the supercooled melt L0 (e.g. Smith & Brown, 1988; Baker & Cahn, 1998; Fig. 13b). In case (2), the composition of the nucleated AFn is controlled by partial equilibrium as expressed by the rule of parallel tangents (e.g. Gusak *et al.*, 2001; Fig. 13c). Therefore, in both cases, nucleation and growth of alkali feldspars more K-rich than at equilibrium can find a thermodynamically sound explanation. However, understanding nucleation requires structural information for both the melt and the nuclei (e.g. Kirkpatrick, 1983). For example, it is unclear why nucleation of a K-rich alkali feldspar should be favored in comparison with a more Na-rich given their similar crystalline structure and chemistry. It is possible that, in hydrous Q-Or-Ab

melts, structural differences between Na- and K-rich parts (Pichavant *et al.*, 1992) and local changes in melt composition (Figs. 9 and 10) can influence compositions of nuclei. Ultimately, interpretation of early alkali feldspar compositions requires more information on the chemistry, size and shape of alkali feldspar nuclei in hydrous haplogranitic melts.

The *second crystallization step* (II) is marked by the appearance of the graphic texture. Only present in the two longest $\Delta T = 120^\circ\text{C}$ charges ($td = 552$ and 1440h , Table 2), the graphic texture follows the appearance of skeletal alkali feldspars. A graphic intergrowth between alkali feldspar and anhedral quartz develops as a network both around the alkali feldspars (Fig. 3a) and in their hollow cores (Fig. 4c). Graphic quartz-alkali feldspar intergrowths and aggregates have been produced in several previous dynamic crystallization studies (London *et al.*, 1989; London, 2014a; London & Morgan, 2017; Sirbescu *et al.*, 2017), sometimes yielding textures remarkably similar to ours (Maneta & Baker, 2014). Grain sizes for both alkali feldspars and quartz are typically micrometric (Fig. 3a), making our graphic texture akin to the granophyric instead of the graphic texture defined by Maneta & Baker (2014). Compositions of graphic intergrowths are overall granitic and dominantly Or-rich (Fig. 7; Table S4). This is consistent with alkali feldspars being K-rich to K-Na intermediate, from $\sim\text{Or}_{75}$ to $\sim\text{Or}_{50}$, in a range identical to the skeletal and polygonal alkali-feldspars analyzed in the 552 and 1440h charges (Table 5). The graphic and granophyric textures of Maneta & Baker (2014) also show a well-marked trend toward potassic bulk compositions.

Quartz saturation in graphic intergrowths (graphic quartz in Fig. 11) is only observed in the $\Delta T = 120^\circ\text{C}$ - $td = 552$ and 1440h charges (Table 2). This corresponds to an effective undercooling of $\sim 90^\circ\text{C}$ since quartz crystallizes $\sim 30^\circ\text{C}$ below the liquidus in our Q-Or-Ab melt composition (Holtz *et al.*, 1992; Fig. S2). Quartz is absent in the $\Delta T = 60^\circ\text{C}$ - $td = 1320\text{h}$ and $\Delta T = 120^\circ\text{C}$ - $td = 120\text{h}$ charges suggesting a kinetic saturation boundary as drawn on Fig. 11. Although rather loosely constrained and referring to graphic quartz and not to free quartz,

quartz saturation $\sim 50^\circ\text{C}$ below the alkali feldspar boundary demonstrates that quartz crystallization in our experiments is slightly more difficult kinetically than alkali feldspar. In Q-Or-Ab-An melts, Swanson (1977) found that larger degrees of undercooling were necessary to nucleate quartz in comparison with plagioclase and (with one exception) alkali feldspar. This is consistent with the general model of less polymerized crystals nucleating faster than more polymerized crystals (Kirkpatrick, 1983).

The graphic texture is one characteristic texture of pegmatites and it has been discussed in many studies (e.g. Lentz & Fowler, 1992; Ikeda *et al.*, 2000; Xu *et al.*, 2015). Fenn (1986) proposed that the graphic texture originates from simultaneous growth of alkali feldspars and quartz in a kinetically driven disequilibrium situation. Alkali feldspar forms first with an initial planar interface that is subsequently disrupted into a cellular one (Fenn, 1986). In general, replacement of planar to cellular interfaces is expected when ΔT increases. Constitutional supercooling (when chemical components are rejected by the growing crystal at the crystal-liquid interface) has the same influence (Kirkpatrick, 1975). Our $\Delta T = 120^\circ\text{C}$ experiments combine the two factors. Rejection of SiO_2 at the alkali feldspar interface is confirmed by our compositional profiles (Figs. 9 and 10). Therefore, development of cellular alkali feldspar and local saturation in SiO_2 are both favored, resulting in quartz saturation and graphic alkali feldspar plus quartz intergrowths. Maneta & Baker (2014) suggested that the presence of Li lowers the degree of undercooling necessary to develop the graphic texture (see also London *et al.*, 1989; Sirbescu *et al.*, 2017). We stress that, in this study performed with a Li-free system, graphic quartz-feldspar intergrowths were obtained for $\Delta T = 120^\circ\text{C}$ and so under conditions not much different from studies performed with additional fluxing components ($\Delta T < 100^\circ\text{C}$, London *et al.*, 1989; $\Delta T = 85^\circ\text{C}$, Maneta & Baker, 2014). In the same way, our graphic textures developed in presence of an aqueous vapor phase (see London *et al.*, 1989). Since ΔT is constant (120°C) in the 120 and 552h charges, it is likely that the

transition from skeletal morphology to graphic alkali feldspar-quartz is the result of constitutional supercooling being enhanced by accumulation of SiO₂ at the interface of growing skeletal alkali feldspars.

The *third crystallization step* (III) is marked by the evolution of the graphic texture to the polymineralic assemblage. In the $\Delta T = 120^\circ\text{C}-td = 552\text{h}$ charge, the polymineralic assemblage has just appeared. The graphic texture passes to the polymineralic assemblage near aggregate margins and, overall, the polymineralic assemblage remains little developed (Fig. 4f). In contrast, in the $\Delta T = 120^\circ\text{C}-td = 1440\text{h}$ charge, the polymineralic assemblage defines the transitional part, i.e. a continuous thick domain at the periphery of the inner part (Fig. 5b). The polymineralic assemblage corresponds to the continuing crystallization of an alkali feldspars-quartz intergrowth in the matrix. Texturally, the polymineralic assemblage and the graphic texture only show second-order differences, suggesting similar conditions of high undercooling. Grain sizes are inframetric in the polymineralic assemblage and micrometric in the graphic texture but the former had less time to grow than the latter. In fact, the main difference between the two associations is chemical. The polymineralic assemblage is much more Na-rich than the graphic texture and it represents mixtures between quartz, albite and minor K-rich or Na-K intermediate alkali feldspars. Albite marks the appearance of a second alkali feldspar phase in the dynamic crystallization sequence. Crystallization of potassic phases during stages I and II drives the melt composition toward progressively higher Na/K as shown by the more sodic melts in the $\Delta T = 120^\circ\text{C}-td = 552\text{h}$ charge (Fig. 8c). Alkali feldspars also become heterogeneous and more albitic (Fig. 6) and the graphic texture evolves toward more Ab-rich compositions near the polymineralic assemblage. A similar sodic trend is apparent in the experiments of London (2014a). This evolution allows nucleation and growth of albite from the supercooled melt in a way analogous to that for Or-rich alkali feldspar during stage I (Fig. 13c). Again, nucleation and growth of kinetically-favored

metastable solid solutions control albite compositions as illustrated by their chemistries ($\sim\text{Or}_{10}$) distinctly more sodic than the Ab-rich branch of the disordered alkali feldspar solvus ($\sim\text{Or}_{18}$, Fig. 6). Appearance of albite in the polymineralic assemblage must go along with continuing crystallization of (most probably) a Na-K intermediate alkali-feldspar to account for bulk intergrowth compositions (Fig. 7).

Development of the polymineralic assemblage is accompanied by textural and compositional changes. At aggregate margins, Na-rich fan crystals substitute to the earlier alkali feldspar crystals and the perthitic texture develops. Alkali feldspars sizes also increase near aggregate rims, as also found in previous studies (London *et al.*, 1989; Maneta & Baker, 2014; Sirbescu *et al.*, 2017). In the same way, the development of albite at the edge of the crystallization front (Maneta & Baker, 2014) and of alkali feldspars with Na- and K-rich sectors have been already described (London *et al.*, 1989; Maneta & Baker, 2014; Sirbescu *et al.*, 2017). The appearance of fan crystals is consistent with the presence of albite in the polymineralic assemblage, and the development of the perthitic texture with alkali feldspars having compositions from inside the solvus at 600°C (Fig. 6). Texturally, the evolution from skeletal to fan morphologies suggests a change of the crystallization mechanism toward lower degrees of undercooling. Fan crystals possess branching geometries (Fig. 4d) characteristic of spherulitic crystals in principle grown at high degrees of undercooling (Lofgren, 1974). However, our fan types differ from typical fibers, being rather coarse-grained and blocky. They are interpreted as planar morphologies analogous to skeletal crystals but crystallized from a H₂O-supersaturated (and more Na-rich) melt (Fig. 10). The effect of H₂O accumulation at concentrations exceeding saturation is to decrease the degree of undercooling at intermediate distances from the alkali feldspar interface (Fig. 12). Lower degrees of undercooling explain the coarsening of grain sizes at aggregate margins as observed in this and other studies since, under these conditions, growth would be favored relative to

nucleation. Therefore, textures suggesting both high ΔT at small distance (polymineralic assemblage) and smaller ΔT at intermediate distance (fan crystals) from the growing aggregate coexist in the $\Delta T = 120^\circ\text{C}$ - $td = 552\text{h}$ charge. Fan crystals are found in the periphery of aggregates (Fig. 4d) and thus appear later than the polymineralic assemblage. Both the fan texture and the coarser grain sizes suggest propagation of a H_2O (and Na) flux out of the aggregate, driven by crystallization during steps I-III. This chemical flux moves diffusively (over distances of $\sim 100\ \mu\text{m}$, Fig. 10) in the melt outward as crystallization progresses and melt is consumed in external parts of the aggregate. This mechanism is probably made possible by the very low T_{Exp} (600°C), which prevents the exsolution of excess H_2O present in the melt as fluid bubbles and the return to equilibrium melt H_2O concentrations. Fluid bubbles are common in the dynamic crystallization charges but there is no indication of progressive fluid exsolution from the center toward the rim of aggregates (Fig. 4). Interface melts (with an assumed excess of 2 wt% H_2O) have viscosities lower by ~ 0.75 log units (corresponding to a lowering of the viscosity to only 15-20% of the original value) than far-field melts using the model of Giordano *et al.* (2008).

The *fourth crystallization step* (IV) controls the formation of the outer part (Fig. 5), the final stage of crystallization of the supercooled melt. It is characterized by large, euhedral and prismatic quartz and subhedral alkali feldspar morphologies. The $\Delta T = 120^\circ\text{C}$ - $td = 1440\text{h}$ charge is the only one where saturation in free quartz (differing from quartz saturation in the graphic texture and polymineralic assemblage) occurs (Fig. 11). Quartz forms the most external and almost monomineralic layer, similar to previous studies (London *et al.*, 1989; London, 2014a; Maneta & Baker, 2014). It is accompanied by alkali feldspars in a slightly more internal position (Fig. 5). These alkali feldspars are perthitic and have K-rich sectors right on the solvus ($\text{Or}_{62}\text{Ab}_{38}$, Fig. 6), although their Na-rich sectors are too Na-rich ($\text{Or}_8\text{Ab}_{92}$, Fig. 6). Texturally, this feldspar is typically coarse and blocky, and differs from alkali

feldspars from earlier crystallization stages. Textures and compositions in the outer part are interpreted as kinetic crystallization products from a melt residual after crystallization of the transitional part. The large grain sizes suggest that growth rather than nucleation was favored. This is the consequence of the crystallization of the polymineralic assemblage in the transitional part which maintains an outward chemical flux of H₂O (Fig. 12) and lowers ΔT in the outer part. We have no information on the H₂O concentration in melts from the outer part since they have been exhausted. However, we speculate that H₂O-supersaturated conditions persisted until crystallization was complete and all H₂O present was transferred to the vapor phase. Therefore, the mechanism envisioned for step IV is basically a continuation of the one initiated during step III. Yet, given the mostly sodic compositions of the polymineralic assemblage (Fig. 7), it is likely that the residual melt during step IV had a slightly lower Na/K than during stage III.

Ripening processes

Several textural features in the dynamic crystallization charges do not fit with a simple mechanism of crystallization of a supercooled melt as detailed above. This includes in particular (1) the polygonal alkali feldspar textural types (Fig. 2d), (2) the euhedral quartz with complex morphologies (Figs. 4b, 5b and 14b), (3) the fan crystals (Fig. 2c) and (4) the megacrysts (Figs. 4a and 5a).

(1) Polygonal crystals are never found exclusive of other alkali feldspar textural types. They coexist with skeletal crystals in the $\Delta T = 60^\circ\text{C}$ - $t_d = 1320\text{h}$ and $\Delta T = 120^\circ\text{C}$ charges (Fig. 11). The association between the polygonal and the skeletal alkali feldspars can be very close and there are textural indications for the skeletal passing progressively to the polygonal type by recrystallization of graphic intergrowths in their hollow cores (Fig. 14a). Polygonal have sizes in the same range as skeletal and fan morphological types (Table 3) and they are

interpreted as former skeletal crystals whose cores have been completely recrystallized. Thus, the polygonal types are the result of two superimposed crystallization mechanisms, successively crystallization from a supercooled melt and textural maturation, more detailed below.

(2) Euhedral quartz with complex morphologies (Q-c) is present both in the $\Delta T = 120^\circ\text{C}$ - $td = 552\text{h}$ and 1440h charges (Figs. 4b, 5b and 14b). These quartz crystals are always surrounded by polygonal alkali feldspars and the graphic texture is never found in-between the touching quartz and feldspar faces. This relation suggests that the Q-c type, as the polygonal alkali feldspars, is the result of the textural maturation of the graphic texture. This mechanism involves redissolution of the smallest particles (i.e., of micrometric feldspar-quartz crystals forming the graphic texture), transport in a surrounding medium and their reprecipitation as larger euhedral feldspar and quartz crystals. The driving force for the ripening process is a reduction of the surface energy of the crystal (e.g. Baronnet, 1984; Voorhees, 1992; Cabane *et al.*, 2005 and references therein). The process contributes to the evolution from skeletal to polygonal crystals and from anhedral quartz (Q-an) to euhedral quartz with complex morphologies (Q-c in Fig. 14b). Thus, ripening of alkali feldspar goes along with ripening of quartz. This later phase precipitates in the voids left between the polygonal crystals giving to the Q-c type its complex morphology (Figs. 4b, 5b and 14b). For the ripening of the graphic texture, melt is most probably the transporting medium despite residual glass being absent in the inner parts of aggregates, as noted above. However, interstitial melt likely remained present during crystallization of skeletal alkali feldspars and of the graphic texture (step II). This implies that textural ripening started early in the inner parts and acted contemporaneously to sequential crystallization.

(3) Fan crystals are found in the transitional part near aggregate rims and are surrounded by melt ($\Delta T = 120^\circ\text{C}$ - $td = 552\text{h}$ charge). These are composite crystals usually

made of several small polygonal units forming different segments but also include large blocky and rough (irregularly surfaced) habits. Fan crystals evolve toward progressively coarser and rough habits (Fig. 14c) interpreted to result from the ripening of small polygonal units in favor of coarser habits with a reduced surface energy. The location of fan crystals near aggregate rims makes the surrounding melt the obvious transporting medium. Thus, the fan (as the polygonal alkali feldspars) types are the result of two superimposed crystallization mechanisms, successively crystallization from a supercooled melt and textural maturation.

(4) Megacrysts are only present in the two $\Delta T = 120^\circ\text{C}$ charges. They have sizes up to several hundred μm (Figs. 4a and 5a), much larger than all other alkali feldspars types and are quite rare, with a maximum of 1-2 individuals per charge. High contrast BSE-SEM imaging reveals that megacrysts are made up of multiple sub-grains, chemically slightly different from each other and with sharp edges (Fig. 14d). Thus, they do not represent a single crystal but can be described as a mosaic of numerous touching alkali feldspars each having the polygonal morphology. Megacrysts are interpreted as products of a complex two-stage ripening process, the first stage involving the maturation of skeletal to polygonal crystals (see above). The second stage is responsible for the assembly of the multiple sub-grains. Note that this occurs without small crystals being present between the polygonal sub-grains (Fig. 14c and d) and, so, the mechanism of textural reequilibration/maturation of polygonal alkali feldspars appears to be unusual. One appealing possibility is abnormal grain growth (AGG) where coarsening of angular crystals occurs by surface-nucleation and leads to exclusive growth of a few large crystals relative to the others (e.g. Kang *et al.*, 2002; Jung *et al.*, 2009; Fisher & Kang, 2019). Although more detailed textural data would be needed on crystal sizes and interface textures between sub-grains, this interpretation accounts for the composite nature, size, distribution and rarity of megacrysts and it strengthens the importance of ripening processes in our experimental charges.

Crystal growth rates

Calculation of crystal growth rates requires, besides information on crystal sizes (Tables 3 and S3), knowledge of the growth duration (t_{gr}). Various approaches have been followed in the literature to estimate this parameter. A growth duration equal to the experimental duration (t_d) was used by Fenn (1977), Baker & Freda (2001) and Maneta & Baker (2014). Maneta & Baker (2014) assumed that crystal growth starts immediately once the experimental temperature is attained. In those studies, all reported growth rates are minimum values; growth rates would be higher if the duration of the nucleation incubation period (t_{nu}) is known so that it can be subtracted from the experimental duration t_d to obtain t_{gr} (Fenn, 1977). Sirbescu *et al.* (2017) determined t_{nu} from time series experiments.

In this study, the growth duration has been obtained from the Temperature-Time-Transformation diagram (Fig. 11) where kinetic saturation boundaries enable t_{nu} to be determined for each experiment. However, our kinetic saturation boundaries are loosely constrained and, so, t_{nu} is associated with significant uncertainties which propagate on t_{gr} ($= t_d - t_{nu}$). For this reason, crystal growth rates (G_L) in this study are order of magnitude estimates. Growth rates for alkali feldspars and quartz were determined from the equation $G_L = (L \cdot l)^{0.5} / t \cdot 2$ where L is the mean length, l the mean width of crystals and t is the growth duration t_{gr} obtained as above (e.g. Bonechi *et al.*, 2020). Note that this assumes that growth continues until the end of the experiment. Another important point is that crystal sizes measured in 2D polished surfaces on BSE-SEM images have been used to calculate growth rates (Table S3). Mathematical methods to correct for 2D to 3D crystal sizes (Couch, 2003; Hammer & Rutherford, 2002) have not been implemented in this study because results are uncertain in the case of hollow, dendritic or skeletal morphologies as in our experiments. The equation above was applied to the calculation of growth rates for skeletal alkali feldspar (AF-

sk) and anhedral quartz (Q-an) from inner parts and to euhedral prismatic quartz (Q-p) from outer parts. Growth rates were not calculated for the Q-c, AF-pol and the megacrysts because: 1) the complex morphology of Q-c types (Figs. 4b and 5b) prevented L and l to be reliably measured and 2) AF-pol and megacrysts both represent matured crystals (see above) and it is not known when growth stopped and maturation started. The alkali feldspar and graphic quartz kinetic saturation boundaries were used to constrain tnu for AF-sk and Q-an respectively and, for Q-p, the free quartz saturation boundary (Fig. 11).

Growth rates from this study are tightly grouped (Table 7) between 7.3×10^{-11} and $1.6 \times 10^{-12} \text{ m s}^{-1}$ and there is no significant difference between alkali feldspar and quartz. Although the number of points is limited, growth rates for skeletal alkali feldspar and anhedral quartz decrease with increasing td . Skeletal alkali feldspar grows at least 6 times faster in the 120h than in the 552h experiment and anhedral quartz at least ~ 25 times faster in the 552h than in the 1440h experiment. In the three $\Delta T = 120^\circ\text{C}$ charges, the growth rate data for skeletal alkali feldspar follow a power law consistent with chemical diffusion in the melt as the growth controlling factor (Figs. 9 and 10). For quartz, the euhedral prismatic type from outer parts grows more than ~ 25 times faster than the anhedral type from inner parts despite identical td (1440h). This is consistent with growth rates being higher as a result of crystallization from a H_2O -supersaturated melt during step IV (see above). Alternatively, euhedral prismatic quartz is likely to have crystallized in a free, presumably vapor-filled, space and there might be an influence of the vapor phase in growth rates in this zone (also marked in the large alkali feldspars).

Alkali feldspar growth rates from this study are at the lower end of the literature data (from 1×10^{-8} to $1 \times 10^{-11} \text{ m s}^{-1}$, Fenn, 1977; Swanson, 1977; Baker & Freda, 2001; Maneta & Baker, 2014; Sirbescu *et al.*, 2017). For quartz, previous growth rate data range from 1×10^{-10} to $1 \times 10^{-12} \text{ m s}^{-1}$ (Swanson, 1977; Baker & Freda, 2001; Sirbescu *et al.*, 2017), overlapping

with results from this study. When comparing these data with ours, it must be remembered that growth rates are specific of textures, as illustrated by the contrasting results for the two quartz textures Q-an and Q-p in the $\Delta T = 120^{\circ}\text{C}$ - $td = 1440\text{h}$ charge. For skeletal alkali feldspars, the slower growth rates in this than in previous studies could be due to overestimated tgr because of textural changes during the experiment. For example, in the $\Delta T = 120^{\circ}\text{C}$ - $td = 552\text{h}$ and 1440h charges, skeletal alkali feldspars grow while the graphic and the polymineralic assemblages develop. It is possible that skeletal growth was slowed because of alkali feldspar crystallization in the graphic and polymineralic domains. If so, growth rate data for the skeletal types in the two charges above would be minimum values. If the corresponding data points are excluded, a positive correlation between growth rate and ΔT is obtained for skeletal alkali feldspars, in agreement with previous studies (Kirkpatrick, 1975; Fenn, 1977; Swanson, 1977).

APPLICATIONS TO PEGMATITE TEXTURES

The dynamic crystallization experiments from this study produced textures that closely resemble natural pegmatites. First, textures of alkali feldspar and quartz characteristic of pegmatites have been obtained. This includes the skeletal and fan alkali feldspar types and the euhedral quartz with complex morphologies which are common in border/wall zones and cores of many pegmatites (Jahns, 1953; Jahns & Burnham, 1969; Jahns, 1982; Černý, 1991; London, 2009; London & Kontak, 2012; London, 2014a). The alkali feldspars megacrysts found in some of our charges resemble the giant crystals found in intermediate zones. Second, polymineralic quartz-feldspar assemblages emblematic of pegmatites such as the graphic texture (Jahns, 1953; Jahns & Burnham, 1969; Jahns, 1982; Černý, 1991; London, 2009; London & Kontak, 2012; London, 2014a) have been reproduced in our experiments. Third, the sequential crystallization texture obtained in the $\Delta T = 120^{\circ}\text{C}$ charges closely simulates

mineral and textural zonations in pegmatites (Jahns, 1953; Jahns & Burnham, 1969; Jahns, 1982; Černý, 1991; London, 2009; London, 2014a). Note that previous experiments, in particular PEG-16 in London (2014a, b), have also succeeded in duplicating a typical pegmatite zonation.

The correspondence between experimental and natural textures is illustrated in [Fig. 15](#). Steps I and II of the experimental sequence (that define the inner parts in [Figs. 4 and 5](#) and are characterized by skeletal alkali feldspars and the graphic texture correspond to border/wall zones of pegmatites (London, 2009; London & Kontak, 2012; London, 2014a). The polymineralic alkali feldspar-quartz assemblage, the fan and perthitic alkali feldspars (step III) together with the coarse perthitic alkali feldspars (step IV) are representative of intermediate (core-margin) zones (London, 2009; London & Kontak, 2012; London, 2014a). The megacrysts are also related to this zone. Last, there is a clear analogy between the monomineralic large prismatic euhedral quartz layer in the most external position during step IV and the quartz cores or quartz crystallized from miarolitic cavities in pegmatites (Jahns, 1953; Jahns & Burnham, 1969; Jahns, 1982; Černý, 1991; London, 2009; London & Kontak, 2012; London, 2014a).

Aplites form characteristic units in pegmatite bodies (e.g. Jahns & Burnham, 1969, Jahns, 1982; London, 1990; Černý, 1991; London, 2009; London, 2014a). Although aplites are not chemically specific, their sodic character has been often emphasized (see London, 2014a for a review). It is tempting to propose a correspondence between aplites and the polymineralic assemblages in the experiments. The sodic bulk compositions, very small (inframetric) grain sizes and the mineralogy (quartz, two alkali feldspars including albite) of experimental polymineralic assemblages reproduce the characteristics of natural aplites. However, albite becomes a major crystallizing phase from step III in the experiments, i.e., relatively late in the sequence. This step III is associated with the intermediate zone ([Fig.](#)

15) whereas aplites are in principle found in a more external position (either near the footwall of the pegmatite or following the wall zone inward, see London, 2014a). In addition, the polymineralic assemblages in our experimental charges show no rhythmic layering, a typical feature of aplites (see London, 2014a for a review). London (2014a) emphasized his PEG-16 as the only known experimental charge resembling a layered aplite.

CONCLUSIONS

Dynamic crystallization combined with equilibrium experiments have been performed on a H₂O-saturated haplogranitic composition at 200 MPa. This combined approach ensured a precise quantification of the various parameters controlling the dynamics of crystallization (T_L , T_{Sol} , ΔT , $\partial T/\partial t$, td). Although only a few parameters have been varied (mainly ΔT and td and both within a limited range), this study provides a framework to explore more fully the dynamics of crystallization of hydrous haplogranitic melts.

Fundamental information has been obtained on nucleation and growth of alkali feldspars and quartz in supercooled hydrous haplogranitic melts. Mineral assemblages and compositions and types of polymineralic assemblages (including the graphic texture) vary systematically with the degree of undercooling (ΔT) and the run duration (td). Compositions of early alkali feldspars (K-enriched) and of late albites (Na-enriched) deviate from those expected at equilibrium. The existence of major element-modified boundary melt layers at the interface of growing feldspar crystals or feldspar-quartz aggregates has been demonstrated. H₂O accumulation at concentrations exceeding saturation is for the first time evidenced and the consequences have been explored for effective undercooling in the melt near the alkali feldspar interface and for interface stability. The new growth rate data obtained for both alkali feldspars and quartz emphasize the importance of textures.

The experimental results allow to discuss recent models for pegmatite genesis (e.g. London, 2014a, b and references therein). *First*, the dynamic crystallization experiments confirm and strengthen liquidus undercooling to generate pegmatite textures (summarized in London, 2014a, b). Our experiments, performed in a F-, B-, Li-free although H₂O-bearing haplogranitic system, demonstrate that the presence of fluxing components is not necessary for the development of pegmatite textures through liquidus undercooling. They also demonstrate that pegmatite textures can be obtained under H₂O-saturated conditions for appropriate ΔT (see London *et al.*, 1989). *Second*, disequilibrium crystallization of the supercooled granitic melt controls textures, phase assemblages and compositions in the pegmatite. This occurs through nucleation and growth of kinetically-favored metastable phases and solid solution compositions. As a result, crystallization is sequential and monomineralic zones are obtained (Figs. 4 and 5). Mineral phases follow a sequence that reflects the magnitude of free energy decreases upon crystallization (London, 2014a, b) but also the kinetics of nucleation in supercooled hydrous granitic melts. Alkali feldspar solid solutions nucleate and grow with out- of-equilibrium compositions (Fig. 6). *Third*, pegmatite textures are the mark of the wide range of thermal regimes and effective ΔT during emplacement and consolidation of the igneous body. Our results illustrate juxtaposition of different ΔT in the same charge because components released into the melt (SiO₂, H₂O) have contrasting influences on effective ΔT (Fig. 12). This has implications for sharp textural variations as seen in pegmatite bodies. Although the role of excluded components has been recognized previously (e.g. London, 2014a and references therein), our results provide the long-expected demonstration of chemical zonation at the alkali feldspar interface in haplogranitic melts (e.g. Fenn, 1986; Maneta & Baker, 2014; Fig. 9). They reveal the existence of a H₂O-supersaturated melt zone at intermediate distances from the growing crystal (Fig. 10) which promotes rapid changes toward larger grain sizes at the front of

graphic zones (e.g. London *et al.*, 2012). *Fourth*, pegmatite consolidation is associated with marked mineralogical variations but comparatively little changes in melt composition. The flux of Na generated by the crystallization of K-rich phases during stages I and II is accommodated by nucleation and growth of albite. Thus, pegmatites provide a rare case where igneous differentiation proceeds through variations in mineralogical modes rather than in liquid compositions. Fluctuations in melt K/Na driven by disequilibrium crystallization of feldspars of contrasting Ab/Or might generate rhythmic layering in pegmatites (Jahns & Burnham, 1969, Jahns, 1982; Černý, 1991; London, 2009; London & Kontak, 2012; London, 2014a). *Fifth*, the ripening processes identified in this study underline the necessity to critically examine all aspects of pegmatite textures (e.g. Kontak & Kyser, 2009). Ripening processes have been generally little considered in previous dynamic crystallization studies (London *et al.*, 1989; Maneta & Baker, 2014; Sirbescu *et al.*, 2017). For example, Maneta & Baker (2014) distinguished between graphic and granophyric alkali feldspars/quartz intergrowths but did not consider the possibility that the granophyric evolves from the graphic by a ripening process, in a way analogous as envisioned above for the graphic texture. Although the ripening processes identified in this study use melt as the transporting medium, the vapor phase may be involved in the origin of the megacrysts and euhedral large prismatic quartz.

ACKNOWLEDGEMENTS

Assistance by O. Rouer on the electron microprobe, by A. Lecomte on the scanning electron microscope (SCMEM-UMR 7359 GeoRessources, Université de Lorraine) and by A. Gurenko and N. Bouden on the secondary ion mass spectrometry (CRPG-UMR 7358, CNRS-INSU, Université de Lorraine) are gratefully acknowledged. E. Le Moing and F. Savoie (ISTO-UMR 7327, Université d'Orléans) helped with the use of the cold-seal pressure vessels.

K.D. thanks gratefully F. Faure (CRPG-UMR 7358, Université de Lorraine) for useful discussions. M. Holness drew our attention to the abnormal grain growth mechanism. The original version of this paper was reviewed by two anonymous reviewers and by David London whose inputs are gratefully acknowledged. Special thanks to one anonymous reviewer for particularly constructive comments and insightful suggestions.

FUNDING

This work was supported by the CESSUR Program of CNRS/INSU and the Agence Nationale de la Recherche (VARPEG Project N° ANR-15-CE01-0001).

SUPPLEMENTARY DATA

Supplementary data for this paper are available at *Journal of Petrology* online.

REFERENCES

- Baker, J.C. & Cahn, J.W. (1998). *Thermodynamics of Solidification*. In: Carter, W.C. & Johnson, W.C. (eds.) The selected works of John W. Cahn. The minerals, metals & material Society, 249-251.
- Baker, D.R. & Freda, C. (2001). Eutectic crystallization in the undercooled Orthoclase-Quartz-H₂O system: experiments and simulations. *European Journal of Mineralogy* **13**, 453-466.
- Baronnet, A. (1984). Growth Kinetics of the silicates - a review of basic concepts. *Fortschritte Der Mineralogie* **62**(2), 187-232.
- Behrens, H. & Nowak, M. (2003). Quantification of H₂O speciation in silicate glasses and melts by IR spectroscopy *-in situ versus* quench techniques. *Phase Transitions* **76**(1-2), 45-61.

- Bonechi, B., Perinelli, C. & Gaeta, M. (2020). Clinopyroxene growth rates at high pressure: constraints on magma recharge of the deep reservoir of the Campi Flegrei Volcanic District (south Italy). *Bulletin of Volcanology* **82**(5).
- Cabane, H., Laporte, D. & Provost, A. (2005). An experimental study of Ostwald ripening of olivine and plagioclase in silicate melts: implications for the growth and size of crystals in magmas. *Contributions to Mineralogy and Petrology* **150**, 37-53.
- Cameron, E.N., Jahns, R.H., McNair, A.H. & Page, L.R. (1949). *Internal structure of granitic pegmatites*. Economic Geology Monograph 2. Economic Geology Publishing CO.
- Černý, P. (1991). Rare-element granitic pegmatites. Part I: Anatomy and internal evolution of pegmatite deposits. *Geoscience Canada* **18**(2), 49-67.
- Couch, S. (2003). Experimental investigation of crystallization kinetics in a haplogranite system. *American Mineralogist* **88**, 1471-1485.
- Faure, F. & Schiano, P. (2005). Experimental investigation of equilibration conditions during forsterite growth and melt inclusion formation. *Earth and Planetary Science Letters* **236**, 882-898.
- Fenn, P.M. (1974). *Nucleation and growth of alkali feldspars from a melt*. In: MacKenzie, W.S. & Zussman, J. (eds.) *The feldspars*. Manchester: Manchester University Press, 360-361.
- Fenn, P.M. (1977). The nucleation and growth of alkali feldspars from hydrous melts. *The Canadian Mineralogist* **15**, 135-161.
- Fenn, P.M. (1986). On the origin of graphic granite. *American Mineralogist* **71**, 325-330.
- Giordano, D., Russell, J.K. & Dingwell, D.B. (2008) Viscosity of magmatic liquids: A model. *Earth and Planetary Science Letters* **271**, 123-134.

- Fisher, J.G. & Kang S-J. L. (2019). Strategies and practices for suppressing abnormal grain growth during liquid phase sintering. *Journal of the American Ceramic Society* **102**, 717-735.
- Gusak, A.M., Hodaj, F. & Bogatyrev, A.O. (2001). Kinetics of nucleation in the concentration gradient. *Journal of physics: Condensed matter* **13**, 2767-2787.
- Hammer, J. E. (2008). *Experimental studies of the kinetics and energetics of magma crystallization*. In: Putirka, K. D. & Tepley, F. J., III (eds.) Minerals, Inclusions and Volcanic Processes. Mineralogical Society of America and Geochemical Society, Reviews in Mineralogy and Geochemistry 69, 9-59.
- Hammer, J.E. & Rutherford, M.J. (2002) An experimental study of the kinetics of decompression-induced crystallization in silicic melt. *Journal of Geophysical Research* **107**(B1-2021), 1-23.
- Holloway, J.R. (1976). Fluids in the evolution of granitic magmas: Consequences of finite CO₂ solubility. *Geological Society of America Bulletin* **87**, 1513-1518.
- Holtz, F., Pichavant, M., Barbey, P. & Johannes, W. (1992). Effects of H₂O on liquidus phase relations in the haplogranite system at 2 and 5 kbar. *American Mineralogist* **77**, 1223-1241.
- Iezzi, G., Mollo, S., Ventura, G., Cavallo, A. & Romano, C. (2008). Experimental solidification of anhydrous latitic and trachytic melts at different cooling rates: The role of nucleation kinetics. *Chemical Geology* **253**, 91-101.
- Iezzi, G., Mollo, S., Torresi, G., Ventura, G., Cavallo, A. & Scarlato, P. (2011). Experimental solidification of an andesitic melt by cooling. *Chemical Geology* **283**, 261-273.
- Ikeda, S., Nakano, T. & Nakashima, Y. (2000). Three-dimensional study on the interconnection and shape of crystals in a graphic granite by X-ray CT and image analysis. *Mineralogical Magazine* **65**(4), 945-959.

- Jahns, R.H. (1953). The genesis of pegmatites. I. Occurrence and origin of giants crystals. *American Mineralogist* **38**, 563-598.
- Jahns, R.H. (1982). *Internal evolution of pegmatite bodies*. In: ˇCerný, P. (ed.) *Granitic Pegmatites in Science and Industry*. Mineralogical Association of Canada Short Course Handbook 8, 293-327.
- Jahns, R.H. & Burnham, C.W. (1969). Experimental studies of pegmatite genesis: I. A model for the derivation and crystallization of granitic pegmatites. *Economic Geology* **64**, 843-864.
- Jung, Y-I., Yoon, D.Y. & Kang S-J. L. (2009). Coarsening of polyhedral grains in a liquid matrix. *Journal of Materials Research* **24**(9), 2949-2959.
- Kang, M-K., Kima, D-Y. & Hwang, N.M. (2002). Ostwald ripening kinetics of angular grains dispersed in a liquid phase by two-dimensional nucleation and abnormal grain growth. *Journal of the European Ceramic Society* **22**, 603-612.
- Kirkpatrick, R.J. (1975). Crystal Growth from the Melt: A Review. *American Mineralogist* **60**, 798-814.
- Kirkpatrick, R.J. (1983). Theory of nucleation in silicate melts. *American Mineralogist* **68**, 66-77.
- Kontak, D.J. & Kyser T.K. (2009). Nature and origin of an LCT-suite pegmatite with late-stage sodium enrichment, Brazil Lake, Yarmouth County, Nova Scotia. II. Implications of stable isotopes ($\delta^{18}\text{O}$, δD) for magma source, internal crystallization and nature of sodium metasomatism. *The Canadian Mineralogist* **47**, 745-764.
- Lee, M.R., Waldron, K.A. & Parsons, I. (1995). Exsolution and alteration microtextures feldspar phenocrysts from the Shap granite. *Mineralogical Magazine* **59**, 63-78.

- Lentz, D.R. & Fowler, A.D. (1992). A dynamic model for graphic quartz-feldspar intergrowths in granitic pegmatites in the southwestern greenville province. *Canadian Mineralogist* **30**, 571-585.
- Lofgren, G. (1974). An experimental study of plagioclase crystal morphology: isothermal crystallization. *American Journal of Science* **274**, 243-273.
- London, D. (1990). *Internal differentiation of rare-element pegmatites; A synthesis of recent research*. In: Stein, H.J. & Hannah, J.L. (eds.) Ore-bearing granite systems; Petrogenesis and mineralizing processes. Geological Society of America Special Paper 246.
- London, D. (1992). The application of experimental petrology to the genesis and crystallization of granitic pegmatites. *The Canadian Mineralogist*, **30**, 499-540.
- London, D. (1999). Melt boundary layers and the growth of pegmatitic textures. *The Canadian Mineralogist* **37**, 826-827.
- London, D. (2005). Granitic pegmatites: an assessment of current concepts and directions for the future. *Lithos* **80**, 281-303.
- London, D. (2009). The origin of primary textures in granitic pegmatites. *The Canadian Mineralogist* **47**, 697-724.
- London, D. (2014a). A petrologic assessment of internal zonation in granitic pegmatites. *Lithos* **184-187**, 74-104.
- London, D. (2014b). Subsolidus isothermal fractional crystallization. *American Mineralogist* **99**, 543-546.
- London, D., (2015). Reply to Thomas and Davidson on "A petrologic assessment of internal zonation in granitic pegmatites" by David London (2014a). *Lithos* **212-215**, 469-484.
- London, D. & Kontak, D.J. (2012). Granitic Pegmatites: Scientific Wonders and Economic Bonanzas. *Elements* **8**(4), 257-261.

- London, D. & Morgan VI, G.B. (2017). Experimental Crystallization of the Macusani Obsidian, with Applications to Lithium-rich Granitic Pegmatites. *Journal of Petrology* **58**(5), 1005-1030.
- London, D., Morgan VI, G.B. & Hervig, R.L. (1989). Vapor-undersaturated experiments with Macusani glass + H₂O at 200 MPa, and the internal differentiation of granitic pegmatites. *Contributions to Mineralogy and Petrology* **102**, 1-17.
- London, D., Morgan VI, G.B., Paul, K.A. & Guttery, B.M. (2012). Internal evolution of miarolitic granitic pegmatites at the little three mine, Ramona, California, USA. *The Canadian Mineralogist* **50**, 1025-1054.
- Maneta, V. & Baker, D.R. (2014). Exploring the effect of lithium on pegmatitic textures: An experimental study. *American Mineralogist* **99**, 1383-1403.
- Martel, C., Dingwell, D.B., Spieler, O., Pichavant, M. & Wilke, M. (2000). Fragmentation of foamed silicic melts: an experimental study. *Earth and Planetary Science Letters* **178**, 47-58.
- Parsons, I. (1969). Subsolidus crystallization behaviour in the system KAlSi₃O₈-NaAlSi₃O₈ - H₂O. *Mineralogical Magazine* **37**(286), 173-180.
- Pichavant, M. (1987). Effects of B and H₂O on liquidus phase relations in the haplogranite system at 1 kbar. *American Mineralogist* **72**, 1056-1070.
- Pichavant, M., Holtz, F. & McMillan, P.F. (1992). Phase relations and compositional dependence of H₂O solubility in quartz-feldspar melts. *Chemical Geology* **96**, 303-319.
- Richet, P., Whittington, A., Holtz, F., Behrens, H., Ohlhorst, S. and Wilke, M. (2000). Water and the density of silicate glasses. *Contributions to Mineralogy and Petrology* **138**, 337-347.
- Rudert, V., Chou, I.M. & Eugster, H.P. (1976). Temperature gradients in rapid-quench cold-seal pressure vessels. *American Mineralogist* **61**, 1012-1015.

- Sirbescu, M.L.C., Schmidt, C., Veksler, I.V., Whittington, A.G. & Wilke, M. (2017). Experimental Crystallization of Undercooled Felsic Liquids: Generation of Pegmatitic Texture. *Journal of Petrology* **58**(3), 539-568.
- Smith, J.V. & Brown, W.L. (1988). *Feldspar minerals. Vol. 1 Crystal Structures, Physical, Chemical, and Microtextural Properties*. Springer-Verlag Berlin, Heidelberg, New York, London, Paris, Tokyo, Second Revised and Extended Edition.
- Swanson, S.E. (1977). Relation of nucleation and crystal-growth rate to the development of granitic textures. *American Mineralogist* **62**, 966-978.
- Thomas, R. & Davidson, P. (2012). Water in granite and pegmatite-forming melts. *Ore Geology Reviews* **46**, 32-46.
- Thomas, R. & Davidson, P. (2015). Comment on "A petrologic assessment of internal zonation in granitic pegmatites" by David London (2014). *Lithos* **212-215**, 462-468.
- Tuttle, O.F. & Bowen, N.L. (1958). Origin of granite in the light of experimental studies in the system NaAlSi₃O₈-KAlSi₃O₈-SiO₂-H₂O. *Geological Society of America Memoir* **74**.
- Voorhees, P.W. (1992). Ostwald ripening of two-phase mixtures. *Annual Review of Materials Science* **22**, 197-215.
- Wen, S. & Nekvasil, H. (1994). SolvCalc: an interactive graphics program package for calculating the ternary feldspar solvus and for two-feldspar geothermometry. *Computers & Geosciences* **20**(6), 1025-1040.
- Xu, H., Zhang, J., Yu, T., Rivers, M., Wang, Y. & Zhao, S. (2015). Crystallographic evidence for simultaneous growth in graphic granite. *Gondwana Research* **27**, 1550-1559.
- Zhang, Y. & Cherniak, D.J. (2010). *Diffusion in Minerals and Melts*. Mineralogical Society of America and Geochemical Society, Reviews in Mineralogy and Geochemistry **72**.

FIGURE CAPTIONS

Fig. 1. Time-temperature path used in the dynamic crystallization experiments and illustration of the main parameters. T_L = liquidus temperature; T_{sol} = solidus temperature; T_{Exp} = dwell temperature; $\Delta T = T_L - T_{Exp}$ (degree of undercooling); $\frac{\delta T}{\delta t}$ = cooling rate; td = duration of the dwell. See text for additional explanations.

Fig. 2. BSE-SEM images showing morphologies of alkali-feldspar (AF) and quartz (Q) in the equilibrium and dynamic experiments. (a) Euhedral tabular alkali feldspars (AF-tab) in glass (L), equilibrium experiment no 9 (Table S2); notice the small size of the crystals. (b) Skeletal alkali feldspar (AF-sk) in glass (L), dynamic experiment 47-3a (Table 2); notice the hollow shape and the dendritic morphologies in the core. (c) Fan alkali feldspar (AF-f) in glass (L), dynamic experiment 43-4b (Table 2). (d) Polygonal alkali feldspar (AF-pol), dynamic experiment 33-4c (Table 2). (e) Large euhedral prismatic quartz (Q-p), dynamic experiment 33-4c (Table 2). A megacryst is also shown. (f) Anhedral quartz (Q-an) surrounded by polygonal alkali feldspars, dynamic experiment 33-4c (Table 2). See Table 3 for additional information. V=Vapor (gas bubble).

Fig. 3. BSE-SEM images of polymineralic associations in the dynamic experiments. (a) Graphic texture, dynamic experiment 43-4b (Table 2), showing alkali feldspars (AF) and quartz (Q-an) intergrowths. (b) Polymineralic assemblage, dynamic experiment 33-4c (Table 2) showing fine-scale mineral intergrowths surrounded by polygonal alkali feldspar (AF-pol), anhedral quartz (Q-an) and euhedral quartz with complex morphologies (Q-c). Albites (edges underlined with white lines) and perthitic alkali feldspar (AF-pt) occur dispersed within the assemblage. The white circles show the locations of EPMA analytical spots (see text). (c) Development of perthitic textures in dynamic experiment 33-4c (Table 2) showing K- and Na-rich streaks and domains. See Table 4 for additional information.

Fig. 4. BSE-SEM images of the $T_{exp} = 600^{\circ}\text{C}$, $\Delta T = 120^{\circ}\text{C}$ - $td = 552\text{h}$ dynamic experiment 43-4b (Table 2). (a) Low-magnification view of the whole half charge showing several crystalline aggregates in glass (L). A megacryst is also present. Arrows indicate zones of mutual contact between aggregates. The bright area is the Au capsule. (b) Higher-magnification view of (a) showing the overall texture of an aggregate with the inner and transitional parts (separated by a dotted line). Large morphologically complex quartz crystals (Q-c), skeletal and polygonal (AF-pol) alkali feldspars are recognizable together with numerous graphic texture zones in the inner part. (c) Detail of the inner part in (b) showing skeletal alkali feldspar (AF-sk) surrounded by graphic texture (GT) zones. Notice the presence of graphic intergrowths in the cores of skeletal crystals and the different quartz morphologies (Q-c and Q-an) and sizes. Glass is absent. (d) Detail of the aggregate rim in (b) showing the transition from skeletal (AF-sk) to fan (AF-f) alkali feldspars. The darkening of crystals reflects the compositional change from skeletal (K-rich) to fan (Na-rich). (e) Appearance of albitic streaks in an alkali feldspar crystal marking an early stage of development of the perthitic texture (AF-pt). (f) Detail of the transition from the inner to the transitional part. The graphic texture (GT) is progressively replaced by the polymineralic assemblage (PA). The overall darkening reflects an evolution from K-rich (graphic texture) to more Na-rich (polymineralic assemblage) compositions (see text and Fig. 7). The white circle shows the location of an EPMA analytical spot for the polymineralic assemblage (see text).

Fig. 5. BSE-SEM images of the $T_{exp} = 600^{\circ}\text{C}$, $\Delta T = 120^{\circ}\text{C}$ - $td = 1440\text{h}$ dynamic experiment 33-4c (Table 2). (a) Low-magnification view of selected fragments representative of the fully crystallized charge. Notice the large megacryst. (b) General texture of a crystallized aggregate showing three parts, inner, transitional and outer (separated by dotted lines). The inner part includes skeletal (AF-sk) and polygonal (AF-pol) alkali feldspars and euhedral

quartz with complex morphologies (Q-c) surrounded by graphic texture (GT) zones. No glass is observed between crystals. Polygonal are more abundant than skeletal morphologies; fan crystals are absent. The transitional part mainly consists of a large (50-150 μm) polymineralic assemblage (PA) matrix. White circles show locations of EPMA analytical spots. The outer part is coarsely crystallized with large quartz crystals showing well faceted prisms and pyramidal terminations (Q-p). Alkali feldspar has a well-developed perthitic texture (AF-pt) and Carlsbad twins.

Fig. 6. Compositions of experimental alkali feldspars. The solvus drawn is calculated from Wen & Nekvasil (1994). See Tables 2 and S2 for experimental conditions and Tables 3 and 4 for abbreviations.

Fig. 7. Normative compositions of electron microprobe analyses of polymineralic associations projected in the Q-Ab-Or diagram (wt%). GT: graphic texture, PA: polymineralic assemblage. Experiments at $T_{Exp} = 600^\circ\text{C}$, $\Delta T = 120^\circ\text{C}$ -td = 552 and 1440h (Table 2). The composition of the starting glass (star), the cotectic curve and the minimum point (m) of the Q-Or-Ab system at 200 MPa under H_2O -saturated conditions (Tuttle & Bowen, 1958) are also shown for reference.

Fig. 8. Normative compositions of glasses from the three types of experiments projected in the Q-Or-Ab diagram (wt%). In the top panel, the cotectic curves of the Q-Or-Ab system at 100, 200 and 400 MPa under H_2O -saturated conditions and the corresponding minimum/eutectic points (Tuttle & Bowen, 1958) are shown together with the starting glass (star). (a) Enlarged view of the shaded portion of (a) showing glass compositions (data in Table 6) in the alkali feldspar-bearing equilibrium experiment 9 (Table S2). The grey star is the composition of the starting glass and the 200 MPa curve is the H_2O -saturated quartz-feldspar cotectic. (b) Glass compositions (data in Table 6) in the three ΔT

= 20°C crystal-free dynamic experiments (*td* as indicated, Table 2). (c) Glass compositions (data in Table 6 and Fig. 9) in the three $\Delta T = 60^\circ\text{C}$ and = 120°C crystal-bearing dynamic experiments (*td* as indicated, Table 2).

Fig. 9. SiO_2 , Al_2O_3 , Na_2O , K_2O (wt%) and A/NK (molar) concentration profiles in glass away from alkali feldspar interfaces (A-B lines in BSE images) in three charges from the dynamic crystallization experiments. (a) $\Delta T = 60^\circ\text{C}$ -*td* = 1320h, (b) $\Delta T = 120^\circ\text{C}$ -*td* = 120h, (c) $\Delta T = 120^\circ\text{C}$ -*td* = 552h. Data from Table 6. On each panel, the horizontal dotted line gives the concentration in the far-field melt (Table 6) and the vertical bar is the standard deviation. A/NK = molar $\text{Al}_2\text{O}_3/(\text{Na}_2\text{O}+\text{K}_2\text{O})$.

Fig. 10. H_2O concentration profiles in glass away from alkali feldspar interfaces (A-B lines in the BSE images of Fig. 9) in three charges from the dynamic crystallization experiments. (a) $\Delta T = 60^\circ\text{C}$ -*td* = 1320h, (b) $\Delta T = 120^\circ\text{C}$ -*td* = 120h, (c) and (d) $\Delta T = 120^\circ\text{C}$ -*td* = 552h (Table 2). In (a), (b) and (c), the H_2O concentrations are determined "by difference" (BD) and in (d) by SIMS. In (a), (b), (c), the horizontal dotted lines give the H_2O concentration determined in the far-field melt (Table 6) and the vertical bar is the standard deviation. In (d), the horizontal solid lines are the H_2O solubilities calculated for 200 MPa at 600 (6.9 wt%) and 800°C (6.4 wt%). See text.

Fig. 11. Temperature-Time-Transformation diagram for the dynamic crystallization experiments summarizing results for different time (*td*) and degrees of undercooling (ΔT , both from Table 2). Crystal-free charges are indicated with open symbols and crystal-bearing charges with solid symbols. Textural annotations are indicated near crystal-bearing charges. L: liquid, AF: alkali feldspar, Q: quartz and other abbreviations as in Table 3 and Fig. 6. Three kinetic saturation boundaries (AF, graphic Q, free Q) are drawn from the experimental data. The location of saturation boundaries constrains the nucleation

incubation period (t_{nu}) and the growth period (t_{gr}) as illustrated on the $\Delta T = 60^\circ\text{C}$ - $td = 1320\text{h}$ charge. See also text.

Fig. 12. Distribution of the undercooling in the melt near the alkali feldspar interface (modified after Kirkpatrick, 1975). The actual T curve represents the temperature decrease away from the interface that results from dissipation of the latent heat of crystallization. The T liquidus curve represents the variation in liquidus temperature as the crystal interface is approached and components more soluble in the melt than in the crystal are rejected (e.g. SiO_2 , Fig. 9). Note the decrease in liquidus temperature at small distance from the interface. The T liquidus curve (H_2O) represents the variation in liquidus temperature that accounts for accumulation of H_2O at the interface at concentrations exceeding saturation (Fig. 10) and for the depressing effect of H_2O on liquidus temperatures. Note the difference between the two T liquidus curves and the influence of H_2O that reduces ΔT at intermediate distances in the melt. ΔT : degree of undercooling; T_{Exp} : dwell temperature; T_L : liquidus temperature. The effect of H_2O accumulation beyond saturation is to decrease the degree of undercooling ΔT (H_2O) at intermediate distances from the interface.

Fig. 13. Crystallization of a hydrous haplogranitic melt. (a) Schematic phase diagram for the H_2O -saturated Q-Or-Ab composition studied projected on the temperature (T)-composition (Ab-Or) plane. The vertical line defines the starting composition (L0). L: liquid; AF: alkali feldspar; TL: liquidus temperature; m: minimum point. The alkali feldspar solvus is shown with AF_{Ab} and AF_{Or} corresponding to alkali feldspars coexisting on the Na-rich and K-rich branches of the solvus respectively. Two temperatures are considered, T1 which is above the solidus and corresponds to a small ($\sim 20^\circ\text{C}$) degree of undercooling (ΔT_1) and T2 below the solidus and which corresponds to a large ($\sim 120^\circ\text{C}$) degree of undercooling

(ΔT_2). L1 and AF1 are respectively the liquid and alkali feldspar coexisting at equilibrium at T1. (b) and (c) Schematic free-energy (G)-composition diagrams corresponding to T=T1 and T=T2 respectively. L(T1) and AF(T1) and L(T2) and AF(T2) are G-composition curves for liquid and alkali feldspar respectively at T1 (b) and T2 (c). In (b), the tangent to the L(T1) G-composition curve at composition L0 is shown (Smith & Brown, 1988; Baker & Cahn, 1998). It intersects the AF(T1) G-composition at AFa and AFb and the interval between these two points defines the range of alkali feldspar compositions whose crystallization will decrease the G of the system compared to the pure liquid. For example, nucleation of alkali feldspar of composition AFn will be associated with a decrease in free energy noted ΔG . Note that AFn is more potassic than AF1 (the equilibrium alkali feldspar composition at T1) and so nucleation of an alkali feldspar more K-rich than the equilibrium composition is possible. In (c), the AF(T2) G-composition curve lies at lower G values than the L(T2) curve. The composition of the nucleating alkali feldspar is defined by the point (AFn) on the AF(T2) curve having its tangent parallel to L0 on the L(T2) curve (Gusak et al., 2001). Note that, in this case, AFn is also more potassic than AF1. Other abbreviations as in (a) and (b).

Fig. 14. Illustration of ripening processes. (a) Formation of a polygonal crystal (AF-pol) by progressive recrystallization of graphic intergrowths in hollow cores of a skeletal crystal (AF-sk), dynamic experiment 43-4b (Table 2). (b) Maturation of the graphic texture (GT) by re-dissolution of the smallest particles of the intergrowths and reprecipitation of larger polygonal alkali feldspar (AF-pol) and euhedral quartz with complex morphology (Q-c). Notice the small anhedral quartz (Q-an) unmodified inside the graphic texture, dynamic experiment 33-4c (Table 2). (c) Detail of the formation of a megacryst from jointing (see arrows) of multiple polygonal crystals (AF-pol) and maturing of fan crystals (AF-f) leading to rough fan morphologies. (d) High contrast BSE image of a megacryst emphasizing its

mosaic texture made up of multiple polygonal crystals (AF-pol). Sub-grains are visible in the center of the megacryst, dynamic experiment 33-4c (Table 2).

Fig. 15. Natural vs. experimental pegmatite textures. The section of a natural pegmatite (modified from Jahns & Burnham, 1969 and London, 2014a) shows the different zones on the right and the corresponding mineralogical/petrological characteristics on the left. The SEM images illustrate experimental textures and mineralogical features from this study. Our experimental charges reproduce several key natural pegmatite textures. Only layered aplites have not been experimentally obtained. See text.

Fig. S1. H₂O concentrations of secondary standard glasses (data in Table S1) and comparison between the four different methods used in this study (SIMS, IR, BD-SIMS, BD-IR) for the determination of glass H₂O contents (See text). The horizontal lines in (a), (b) and (d) are Karl-Fischer titration (KFT) data (Holtz *et al.*, 1992) drawn as reference. (a): glass 1, (b): glass 5, (c): glass 2, (d): glass 38. The glass # refers to the run # in Table S2.

Fig. S2. Temperature (°C) vs. H₂O in melt (%) diagram summarizing the phase equilibrium results for composition Q₃₀Or₃₂Ab₃₈ at 200 MPa. See text for the determination of H₂O contents. Horizontal bars are individual standards deviations. Lines are field boundaries hand-drawn from the experimental data points. Abbreviations: Q=quartz; L=liquid; AF=alkali feldspar; V=vapor. Note that the vapor present fields are shown restricted to H₂O-saturated conditions.

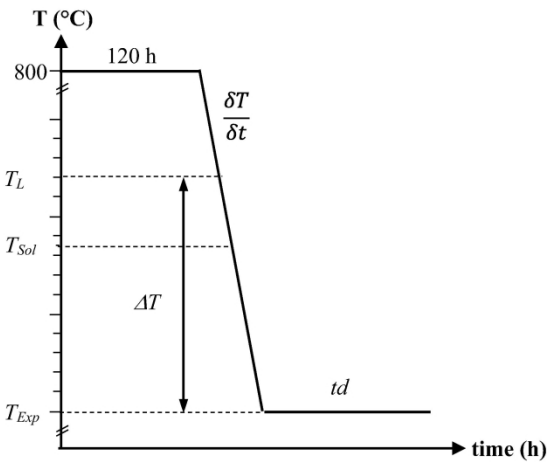


Fig. 1.

112x188mm (600 x 600 DPI)

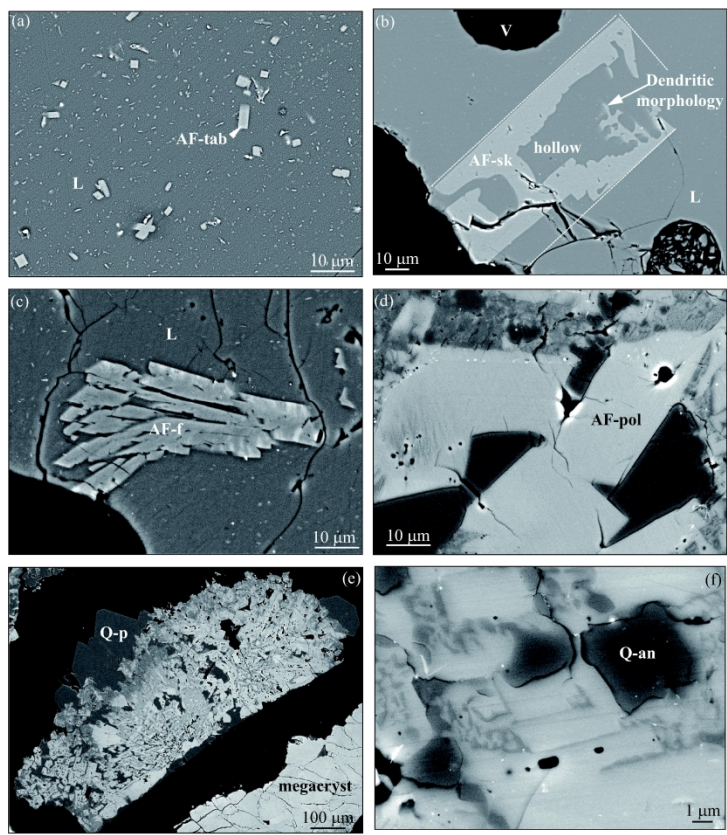


Fig. 2.

190x275mm (600 x 600 DPI)

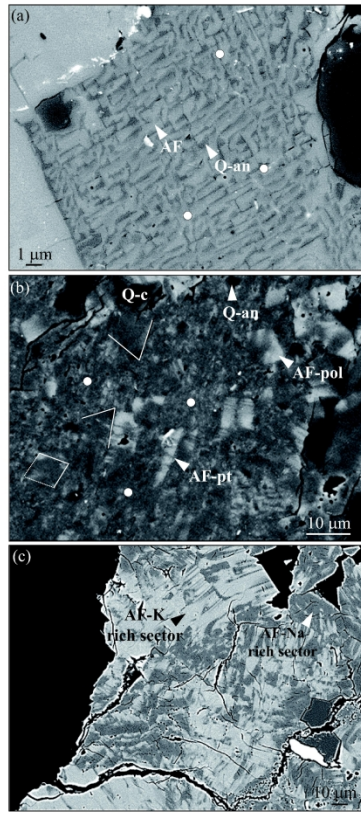


Fig. 3.

190x275mm (600 x 600 DPI)

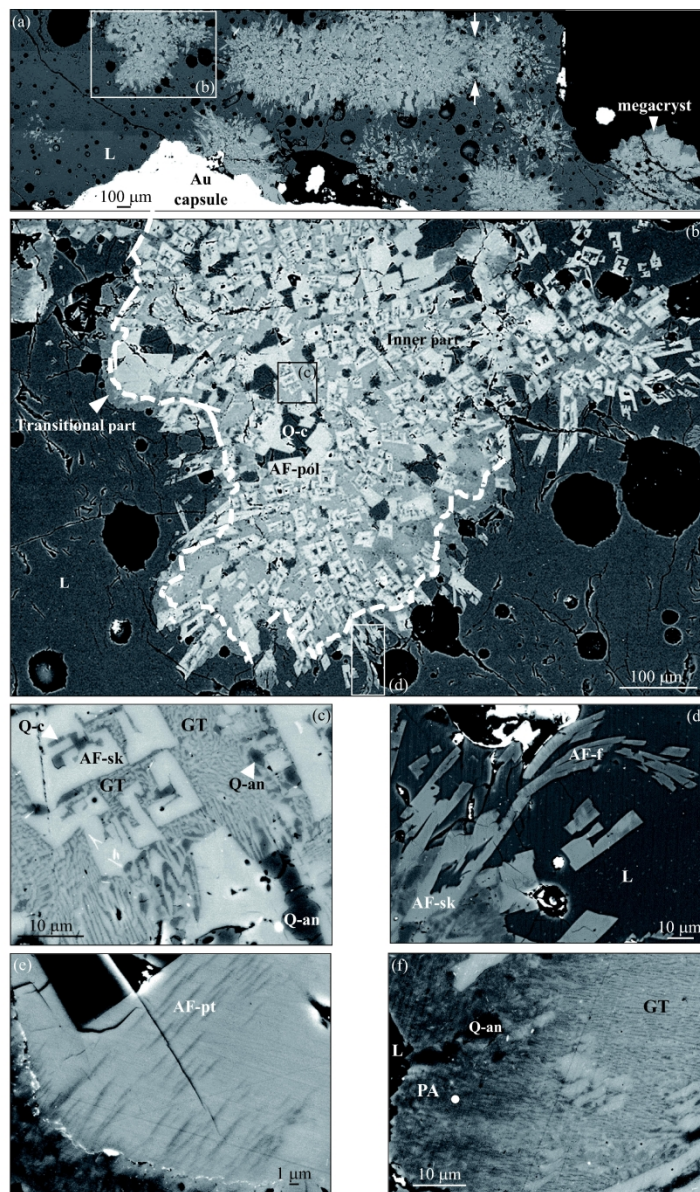


Fig. 4.

190x275mm (600 x 600 DPI)

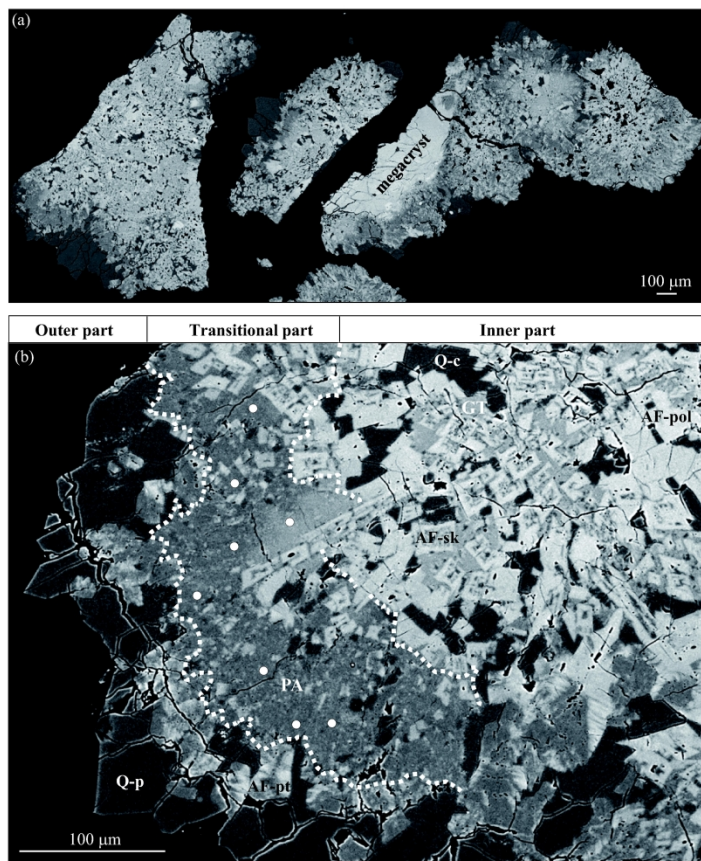


Fig. 5.

190x275mm (600 x 600 DPI)

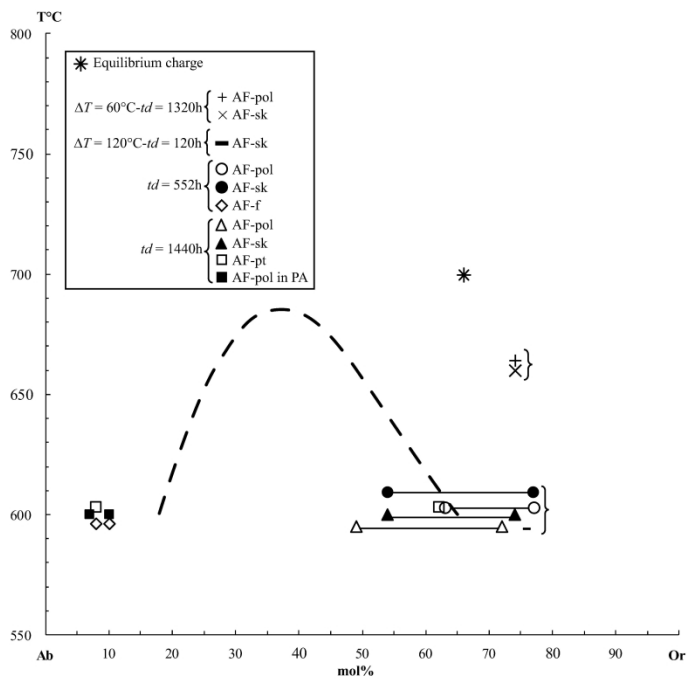


Fig. 6.

212x297mm (600 x 600 DPI)

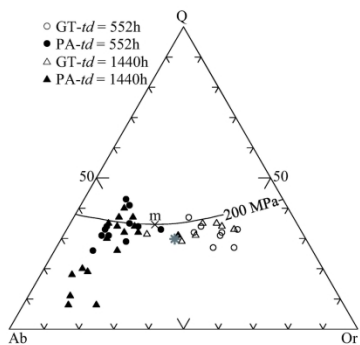


Fig. 7.

190x275mm (300 x 300 DPI)

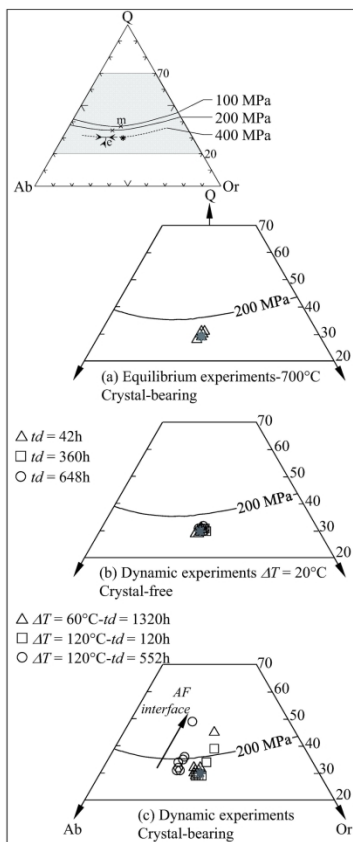


Fig. 8.

190x275mm (300 x 300 DPI)

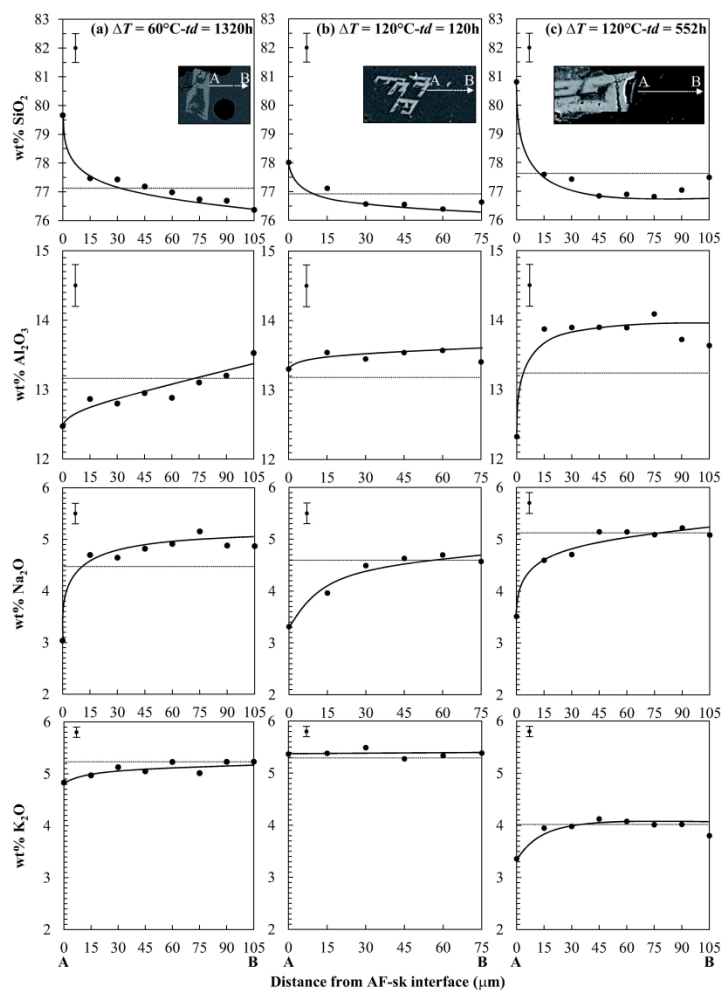


Fig. 9.

190x275mm (600 x 600 DPI)

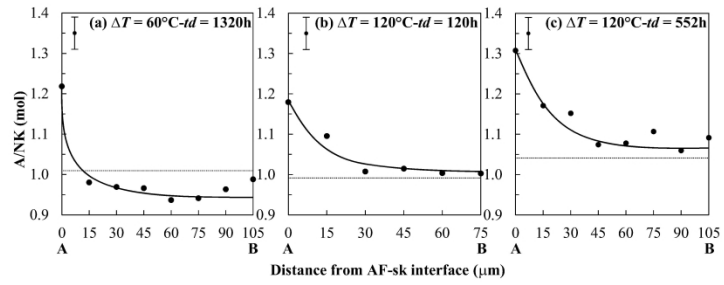


Fig. 9. (continued)

190x275mm (600 x 600 DPI)

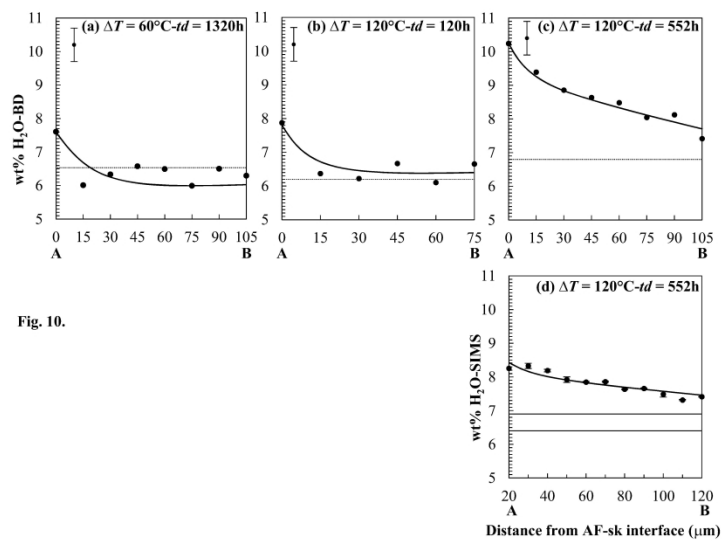


Fig. 10.

190x275mm (600 x 600 DPI)

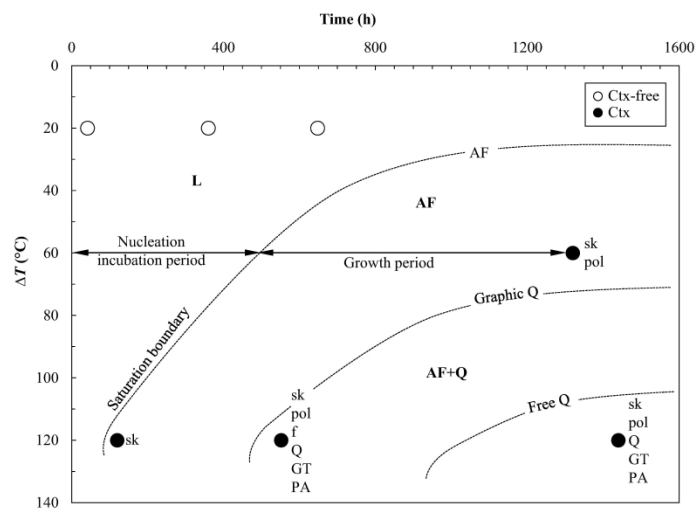


Fig. 11.

190x275mm (600 x 600 DPI)

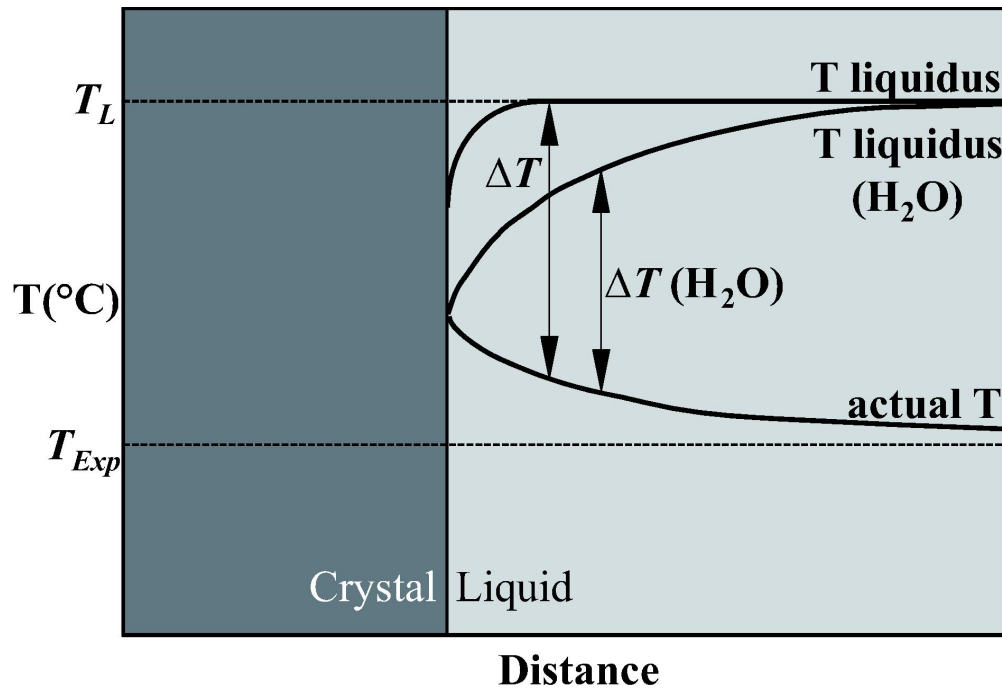


Fig. 12.

80x62mm (600 x 600 DPI)

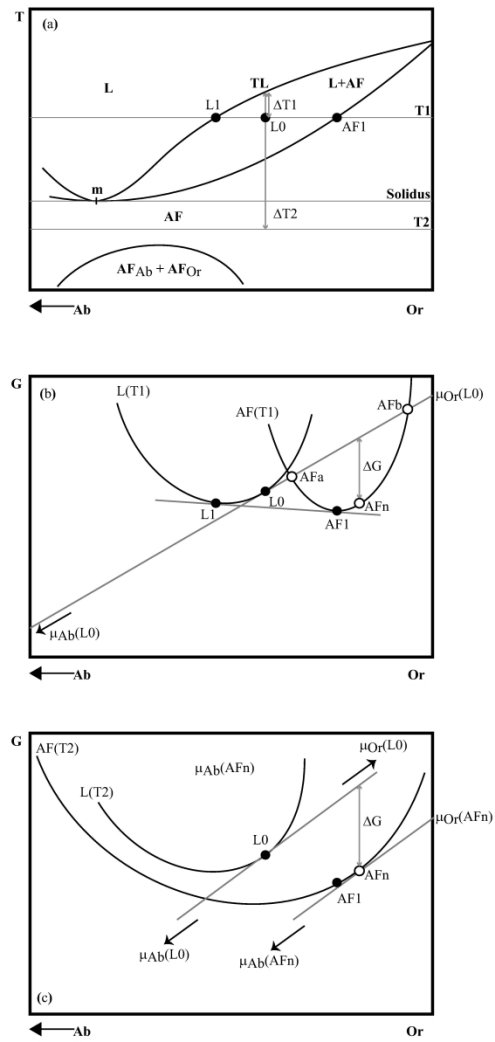


Fig. 13.

199x300mm (600 x 600 DPI)

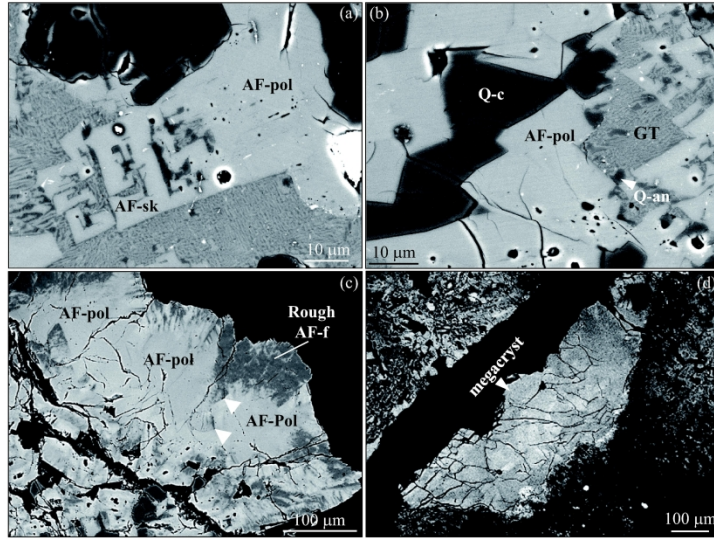


Fig. 14.

190x275mm (600 x 600 DPI)

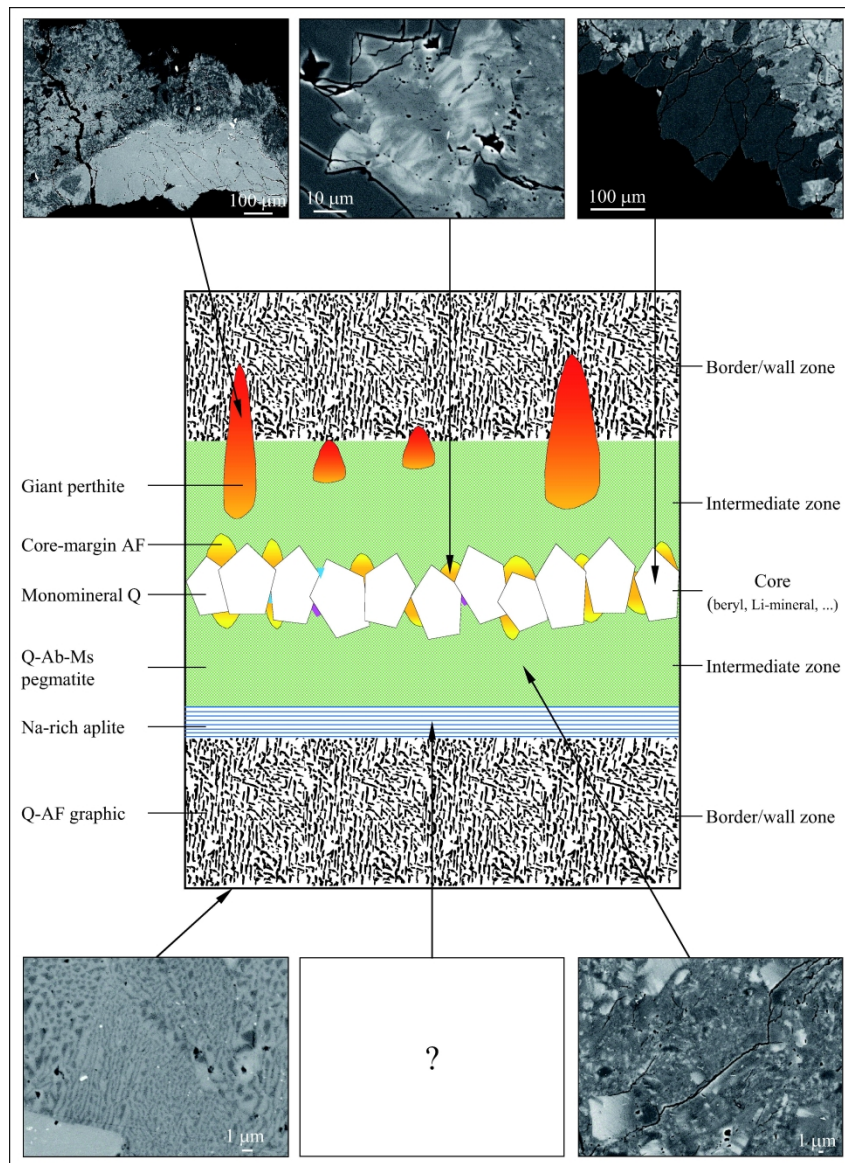


Fig. 15.

160x226mm (600 x 600 DPI)

Table 1: Chemical and CIPW normative composition of the starting glass

Oxide	wt %	CIPW norm	wt%
SiO ₂	75.81 (0.37)	Q	29.42
Al ₂ O ₃	13.20 (0.15)	Or	32.43
Na ₂ O	4.49 (0.18)	Ab	38.07
K ₂ O	5.23 (0.10)	NaS	0.08
Total	98.73 (0.41)		

Data are averages and standard deviations (numbers in brackets) of 25 electron microprobe analyses. Glass labeled after its normative Q/Or/Ab contains approximately 30% Q, 32% Or, 38% Ab (abbreviated Q₃₀Or₃₂Ab₃₈). NaS: normative Na₂SiO₃.

Table 2: Conditions and results of the dynamic crystallization experiments

Run no	T_{Exp} (°C)	ΔT (°C)	$\frac{\delta T}{\delta t}$ (°C/min)*	td (h)	Phase assemblage	Morphologies		Textures
						AF	Q	
25-2a	700	20	~5	42	L	-	-	
21-2b	700	20	~5	360	L	-	-	
29-2c	700	20	~5	648	L	-	-	
47-3a	660	60	~3.5	1320	L-AF	sk, pol		
48-4a	600	120	~7	120	L-AF	sk		
43-4b	600	120	~7	552	L-AF**-Q	sk, pol, f	an, c	GT, PA, pt
33-4c	600	120	~7	1440	L(?) - AF**-Q	sk, pol	an, c, p	GT, PA, pt

All experiments performed at 2 kbar under H₂O-saturated conditions. T_{Exp} : experimental (dwell) temperature; ΔT : degree of undercooling ($T_L - T_{Exp}$); $\delta T/\delta t$: rate of the cooling ramp; td : duration of the dwell. See Fig. 1 for illustration. *cooling rates apply to the first half part of the cooling ramp. For the last and final parts, cooling rates are slower (see text).

L: liquid (silicate melt); AF: alkali feldspar; Q: quartz. AF** two alkali feldspars present. A vapor phase is present in all charges.

sk: skeletal; pol: polygonal; f: fan; an: anhedral; c: complex morphology; p: prismatic morphology.

GT: graphic texture; PA: polymineralic assemblage; pt: perthitic texture.

Table 3: Crystal morphologies and sizes

Crystalline Phase	Description	Abbr.	Fig.	Long axis (L)				Short axis (l)			
				Length (μm)		Mean	n	Length (μm)		Mean	n
				Min	Max			Min	Max		
AF	Tabular (tab): small euhedral flattened crystals (Lofgren, 1974)	AF-tab	2a	1	12	5 (2)	24	1	4	2 (1)	24
AF	Skeletal (sk): hollow crystal; most have hollows in filled with dendritic morphologies (Lofgren, 1974)	AF-sk	2b	16	119	57 (28)	40	5	44	19 (8)	40
AF	Fan (f): composite crystal made of several polygonal units forming different segments, some straight and others branched and curved; general shape similar to a fan, a spherulitic morphology defined by Lofgren (1974); includes coarse and rough variants	AF-f	2c	32	113	56 (29)	8	6	40	24 (20)	8
AF	Polygonal (pol): filled crystals with well-developed faces and euhedral shape	AF-pol	2d	5	80	36 (17)	44	4	50	19 (9)	44
Q	Euhedral crystal with well-developed but morphologically complex faces (c)	Q-c	4b	4	135	53 (26)	32	1	70	26 (12)	32
Q	Euhedral large prismatic crystal with well-developed faces (p)	Q-p	2e	47	240	145 (81)	6	23	180	98 (64)	6
Q	Anhedral crystal lacking well-developed faces and geometrical shape (an)	Q-an	2f	3	68	23 (20)	12	2	34	11 (10)	12

AF: alkali feldspar; Q: quartz.

Max., length of the long axis; Min., length of the short axis; Mean, average of the data; n, number of measured crystals; numbers in brackets indicate standard deviations (1σ).

Sizes for the tabular morphology determined on the 700°C equilibrium charge and for the other morphologies on the $\Delta T = 120^\circ\text{C}$ -td = 552 and 1440h charges (See Table 2; S2). Averages include data from the different charges (see Table S3).

Table 4: Polymineralic associations

Mineral assemblage	Description	Abbreviation	Fig.
Q-AF	Graphic: micrometric crystallographically oriented quartz-feldspar intergrowths; alkali-feldspars dominantly K-rich to K-Na intermediate	GT	3a
Q-AF	Infra-micrometric polymineralic aggregate of quartz and feldspars; alkali-feldspars dominantly Na-rich but two alkali-feldspars, one Na-rich and the other K-Na intermediate, can be present	PA	3b
AF-AF	Perthitic: composite alkali feldspar made of Na- and K-rich streaks or domains	AF-pt	3c

Table 5: Representative electron-microprobe analyses of alkali feldspars

Equilibrium experiments			Dynamic crystallization experiments																			
ΔT (°C)	0	60	120													1440						
T_{Exp} (°C)	700	660	600																			
td (h)	120	1320	120			552						1440										
Run no.	9	47-3a	48-4a			43-4b						33-4c										
Morphology	AF-tab	AF-sk	AF-pol	AF-sk	AF-sk	AF-sk	AF-f	AF-pol	AF-pol	AF-pol in megacryst	AF-pol in megacryst	Rough AF-f	AF-sk	AF-sk	AF-pol	AF-pol	AF-pol in megacryst	AF-pol in megacryst	Large Or-rich	AF-pt Ab-rich	AF-pol in PA*	AF-pol in PA*
n	1	6	5	1	1	1	1	1	1	1	1	1	1	1	1	1	1	1	1	1	1	1
wt%																						
SiO ₂	67.23	64.33 (0.43)	64.51 (0.26)	68.47	65.83	66.57	69.02	65.54	67.09	65.72	65.97	67.50	66.70	66.79	66.46	67.46	65.33	66.30	66.25	68.58	69.92	69.91
Al ₂ O ₃	17.29	17.60 (0.25)	17.47 (0.14)	15.40	17.75	17.72	18.16	17.95	17.46	18.00	17.31	18.72	17.48	18.12	17.41	18.08	18.15	18.22	18.44	19.30	19.28	19.20
Na ₂ O	3.84	2.89 (0.07)	2.89 (0.07)	2.20	2.51	5.16	9.89	2.68	4.11	3.47	4.13	10.43	2.86	5.26	3.16	5.56	2.67	4.79	4.33	10.54	9.23	9.83
K ₂ O	11.24	12.62 (0.13)	12.57 (0.03)	10.86	12.84	9.27	1.70	13.34	10.60	11.76	10.45	1.47	12.66	9.53	12.07	8.20	13.16	9.4	10.79	1.48	1.57	1.06
Total	99.60	97.44 (0.50)	97.44 (0.31)	96.93	98.93	98.72	98.77	99.51	99.26	98.94	97.86	98.12	99.70	99.70	99.09	99.30	99.29	98.71	99.82	99.91	100	100
Cations for 8 O oxygens																						
Si	3.06	3.02	3.02	3.16	3.03	3.04	3.05	3.01	3.05	3.02	3.05	3.01	3.05	3.02	3.05	3.04	3.01	3.02	3.01	3.01	3.04	3.04
Al	0.93	0.97	0.96	0.84	0.96	0.95	0.95	0.97	0.94	0.97	0.94	0.99	0.94	0.97	0.94	0.96	0.98	0.98	0.99	1.00	0.99	0.98
Na	0.34	0.26	0.26	0.20	0.22	0.46	0.85	0.24	0.36	0.31	0.37	0.90	0.25	0.46	0.28	0.49	0.24	0.42	0.38	0.90	0.78	0.83
K	0.65	0.75	0.75	0.64	0.75	0.54	0.10	0.78	0.62	0.69	0.62	0.08	0.74	0.55	0.71	0.47	0.77	0.55	0.63	0.08	0.09	0.06
Or (mol%)	66	74	74	76	77	54	10	77	63	69	62	8	74	54	72	49	76	56	62	8	10	7

See Tables 2 and S2 for experimental details.

See Tables 2 and 3 for abbreviations.

* SEM-EDS analyses of AF-pol in polymineralic assemblage (PA) (see text).

For AF-sk, AF-pol, AF-pol in megacryst and AF-pol in PA in charges 43-4b and 33-4c, the two analyses correspond to the maximum and minimum of the Or compositional range.

=number of analyses. When multiple analyses are available, the average is given together with standard deviations (1 σ) in wt% (numbers in brackets).

Or (mol%) = 100xK/(Na+K) at.

Table 6: Representative electron microprobe analyses of glasses

Equilibrium experiments					Dynamic crystallization experiments														
ΔT (°C)	0				20			60				120			120				
T_{Exp} (°C)	850	800	750	700	700			660				600			600				
td (h)	120	120	120	120	42	360	648	1320				120			552				
Run no.	17	1	5	9	25-2a	21-2b	29-2c	47-3a				48-4a			43-4b				
								Inside AF-sk	Near AF-sk	Away from AF-sk	Far-field melt		Near AF-sk	Away from AF-sk	Far-field melt		Near AF-sk	Away from AF-sk	Far-field melt
n	8	64	40	8	6	7	7	1	1	1	24		1	1	14		1	1	18
wt%																			
¹ SiO ₂	76.50 (0.29)	77.08 (0.35)	77.13 (0.19)	76.88 (0.31)	76.57 (0.15)	76.53 (0.23)	76.67 (0.18)	82.13	79.66	76.37	77.13 (0.39)		78.01	76.64	76.92 (0.19)		80.81	77.48	77.63 (0.34)
Al ₂ O ₃	13.28 (0.13)	13.20 (0.21)	13.18 (0.17)	12.93 (0.16)	13.02 (0.18)	12.91 (0.09)	12.95 (0.20)	11.20	12.47	13.53	13.16 (0.14)		13.30	13.40	13.18 (0.18)		12.32	13.63	13.23 (0.27)
Na ₂ O	4.81 (0.16)	4.44 (0.21)	4.47 (0.21)	4.96 (0.20)	5.06 (0.13)	5.12 (0.21)	5.03 (0.22)	2.20	3.04	4.87	4.48 (0.32)		3.31	4.57	4.61 (0.16)		3.51	5.08	5.12 (0.20)
K ₂ O	5.40 (0.12)	5.28 (0.09)	5.23 (0.08)	5.23 (0.10)	5.34 (0.08)	5.44 (0.10)	5.35 (0.05)	4.48	4.83	5.23	5.23 (0.13)		5.37	5.38	5.29 (0.09)		3.36	3.80	4.02 (0.12)
Total	100	100	100	100	100	100	100	100	100	100	100		100	100	100		100	100	100
H ₂ O	6.3 (0.3)	5.83* (0.02)	6.50* (0.00)	6.8 (0.3)	6.4 (0.2)	6.4 (0.3)	5.9 (0.2)	7.1	7.6	6.3	6.5 (0.3)		7.8	6.6	6.2 (0.5)		10.2	7.4	6.8 (0.6)
A/NK (mol)	0.96 (0.02)	1.01 (0.03)	1.01 (0.04)	0.93 (0.02)	0.92 (0.02)	0.90 (0.03)	0.92 (0.04)	1.32	1.22	0.99	1.01 (0.06)		1.18	1.00	0.99 (0.03)		1.31	1.09	1.04 (0.04)
CIPW norm (wt%)																			
Q	29.3	31.0	31.1	30.6	29.9	30.1	30.2	52.2	43.5	28.4	31.1		38.2	29.4	30.3		47.5	33.4	32.5
Or	31.9	31.2	30.9	30.9	31.6	32.1	31.6	26.5	28.5	30.9	30.9		31.7	31.8	31.3		19.8	22.5	23.8
Ab	38.2	37.6	37.8	37.4	37.2	36.1	36.8	18.6	25.7	40.4	37.9		28.0	38.7	38.3		29.7	43	43.3
NaS	0.6	0.0	0.0	1.1	1.3	1.7	1.3	0.0	0.0	0.2	0.0		0.0	0.0	0.2		0.0	0.0	0.0
C	0.0	0.2	0.2	0.0	0.0	0.0	0.0	2.7	2.2	0.0	0.1		2.0	0.1	0.0		2.9	1.1	0.5

See Tables S2 and 2 for experimental details.

See Table 3 for abbreviations.

"Inside AF-sk": individual analysis (hollow of Fig. 2b); "Near AF-sk" and "Away from AF-sk": respectively first and last analysis of compositional profiles (Figs. 9 and 10); "Far-field melt": average of multiple analyses in crystal-free zones (dotted lines on Figs. 9 and 10).

n = number of analyses. When multiple analyses are available, the average is given together with standard deviations (1σ) in wt% (numbers in brackets).

¹Oxide concentrations are electron microprobe data normalized to 100% H₂O-free. *H₂O contents determined by SIMS. For the others, H₂O contents are calculated from "by difference"-SIMS (see text) with an uncertainty of $\pm 0.5\%$ absolute. A/NK = molar Al₂O₃ / (Na₂O + K₂O).

NaS = normative Na₂SiO₃. C = normative corundum.

Table 7: Growth durations and crystal growth rates in 2D polished surfaces on BSE-SEM images

ΔT (°C)	60	120					
td (h)	1320	120	552	1440	552	1440	1440
Morphology	AF-sk	AF-sk			Q-an		Q-p
*L (μm)	111	27	68	46	31	15	145
*l (μm)	50	21	21	18	14	8	98
** tgr (h)	845	45	477	1365	77	965	415
*** G_L (m s^{-1})	1.2×10^{-11}	7.3×10^{-11}	1.1×10^{-11}	2.9×10^{-12}	3.7×10^{-11}	1.6×10^{-12}	3.9×10^{-11}

*L: long axis of the crystal. *l: short axis of the crystal. For $\Delta T = 60^\circ\text{C}$ and 120°C - $td = 120\text{h}$, only one L and l values are available. For all others, mean L and l values have been used (see Table S3).

** tgr : growth duration determined from Fig. 11 (see text).

*** G_L : crystal growth rate calculated as $(L \cdot l)^{0.5} / tgr^2$.